The Astrophysical Journal, 984:25 (18pp), 2025 May 1 https://doi.org/10.3847/1538-4357/adbbb9

PSZ2 G181.06+48.47. II. Radio Analysis of a Low-mass Cluster with Exceptionally Distant Radio Relics

Kamlesh Rajpurohit[1], Andra Stroe[1,2], Ewan O'Sullivan[1], Eunmo Ahn[3], Wonki Lee[3], Hyejeon Cho[3,4], M. James Jee[3,5], Reinout van Weeren[6], Lorenzo Lovisari[1,7], Kyle Finner[8], Aurora Simionescu[9], William Forman[1], Timothy Shimwell[6,10], Christine Jones[1], Zhenlin Zhu[1,11,12], and Scott Randall[1]
[1] Center for Astrophysics | Harvard & Smithsonian, 60 Garden St., Cambridge, MA 02138, USA; kamlesh.rajpurohit@cfa.harvard.edu
[2] Space Telescope Science Institute, 3700 San Martin Drive, Baltimore, MD 21218, USA
[3] Department of Astronomy, Yonsei University, 50 Yonsei-ro, Seodaemun-gu, Seoul 03722, Republic of Korea
[4] Center for Galaxy Evolution Research, Yonsei University, 50 Yonsei-ro, Seodaemun-gu, Seoul 03722, Republic of Korea
[5] Department of Physics and Astronomy, University of California, Davis, One Shields Avenue, Davis, CA 95616, USA
[6] Leiden Observatory, Leiden University, PO Box 9513, NL-2300 RA Leiden, The Netherlands
[7] INAF, Istituto di Astrofisica Spaziale e Fisica Cosmica di Milano, via A. Corti 12, 20133 Milano, Italy
[8] IPAC, California Institute of Technology, 1200 E California Blvd., Pasadena, CA 91125, USA
[9] SRON, Netherlands Institute for Space Research, Sorbonnelaan 2, 3584 CA Utrecht, The Netherlands
[10] ASTRON, the Netherlands Institute for Radio Astronomy, Postbus 2, NL-7990 AA Dwingeloo, The Netherlands
[11] SRON Netherlands Institute for Space Research, Niels Bohrweg 4, 2333 CA Leiden, The Netherlands
[12] Leiden Observatory, Leiden University, Niels Bohrweg 2, 2300 RA Leiden, The Netherlands
Received 2025 January 12; revised 2025 February 20; accepted 2025 February 24; published 2025 April 22

Abstract

We report upgraded Giant Metrewave Radio Telescope and Karl J. Jansky Very Large Array radio observations of a low-mass merging galaxy cluster PSZ2 G181.06+48.47. This exceptional galaxy cluster hosts two megaparsec-scale diffuse sources, symmetrically located with respect to the cluster center and separated by about 2.6 Mpc in projection. We detect these low surface brightness sources in our new high-frequency observations (0.3–2 GHz) and classify them as radio relics associated with merger-driven shock fronts. The southwest relic exhibits an inverted morphology and shows evidence of spectral steepening in the post-shock region, potentially tracing a high Mach number shock ($\sim$4) under the framework of diffusive shock acceleration. The northeast relic is found to be highly polarized with a 22% average polarization fraction at 1.5 GHz and aligned magnetic field vectors. Its spectral and polarization properties, along with the presence of a nearby tailed galaxy, support reacceleration scenarios. The merger axis defined by the two relics is tilted by $\sim$45° with respect to the plane of the sky, which implies an unprecedented physical separation of $\sim$3.5 Mpc. We also detect a possible faint radio halo, suggesting weak turbulence in the central cluster region. We conclude that the faint double relics can be best explained by two outward-moving shock waves in which particles are (re)accelerated and that the cluster is in an evolved merger state. PSZ2 G181.06+48.47 presents a unique opportunity to investigate particle acceleration in low-mass systems characterized by large relic separations.

Unified Astronomy Thesaurus concepts: Non-thermal radiation sources (1119); Radio continuum emission (1340); Galaxy clusters (584); Large-scale structure of the universe (902); Extragalactic radio sources (508)

1. Introduction

Galaxy clusters grow through accretion and via mergers of smaller galaxy clusters and groups. During mergers, large-scale shocks are driven into the intracluster medium (ICM), forming radio relics at cluster outskirts (see, e.g., G. Brunetti & T. W. Jones 2014; R. J. van Weeren et al. 2019, for a theoretical and observational review). The detection of X-ray discontinuities/edges at the location of the relics confirms the connection between radio relics and ICM shocks (M. Markevitch & A. Vikhlinin 1997; C. L. Sarazin et al. 2013; A. Botteon et al. 2016; T. W. Shimwell et al. 2015). Relics have typically steep radio spectra[13] ($\alpha \leqslant -1$) and are among the strongest linearly polarized sources in the sky, reaching polarization fractions as high as 60% (>1 GHz), with magnetic field orientations well aligned with the shock surface (e.g., R. J. van Weeren et al. 2010; A. Bonafede et al. 2012; F. N. Owen et al. 2014; D. Wittor et al. 2019; G. Di Gennaro et al. 2021; P. Domìnguez-Fernández et al. 2021; K. Rajpurohit et al. 2022a).

Radio relic sizes, morphology, and separations from the cluster center vary significantly, as does their degree of association with shocks detected via X-ray observations. This makes it challenging to obtain a self-consistent theoretical model of the origin of relics. According to the most widely accepted scenario (e.g., G. Brunetti & T. W. Jones 2014; R. J. van Weeren et al. 2019; S. Paul et al. 2023), radio relics originate when particles at the shock front are accelerated via diffusive shock acceleration (DSA) mechanisms (L. O. Drury 1983; M. Hoeft & M. Brüggen 2007). However, the acceleration efficiency of weak ICM shocks ($\mathcal{M} \leqslant 2.5$) appears too low to explain the high luminosity of many relics, if the particles are accelerated directly from the thermal ICM (A. Botteon et al. 2020). Alternative models include shock reacceleration, where shocks reaccelerate fossil electrons previously injected by active galactic nuclei

[13] We define the spectral index, α, so that $S_\nu \propto \nu^\alpha$, where S is the flux density at frequency ν.

(AGN; H. Kang & D. Ryu 2011, 2016; A. Stroe et al. 2014, 2016; H. Kang 2016), or a multiple-shock scenario (MSS; e.g., H. Kang 2021; G. Inchingolo et al. 2022). Both models help reconcile the lower acceleration efficiency with the high radio luminosity for weak-shock relics (A. Bonafede et al. 2014; R. J. van Weeren et al. 2017; G. Di Gennaro et al. 2018).

Mergers between galaxy clusters can also produce another type of steep-spectrum diffuse radio source, known as a radio halo, which fills the central regions of clusters and typically follows the thermal ICM morphology (G. Giovannini & L. Feretti 2004; A. Bonafede et al. 2013; A. Bonafede et al. 2022; A. Botteon et al. 2022; K. Rajpurohit et al. 2021a). Halos are believed to be produced by reacceleration of (primary or secondary) particles via stochastic Fermi II−type processes driven by cluster-merger-induced ICM turbulence (G. Brunetti et al. 2001; V. Petrosian 2001; G. Brunetti & A. Lazarian 2007). Radio halos are also characterized by their steep spectral indices, namely $\alpha \leqslant -1.1$, and are usually unpolarized (e.g., R. J. van Weeren et al. 2012; D. N. Hoang et al. 2018; A. Wilber et al. 2018; A. Botteon et al. 2020; L. Bruno et al. 2021; K. Rajpurohit et al. 2021a; A. Bonafede et al. 2022; S. P. Sikhosana et al. 2023). The radio power (at 1.4 GHz and 144 MHz) of halos is found to increase with the host cluster mass; therefore, it is challenging to detect faint radio halos in low-mass clusters. Only a handful of radio halos are detected in clusters with mass $M_{500} \leqslant 5 \times 10^{14}\, M_{\odot}$ (e.g., K. Knowles et al. 2016; S. Paul et al. 2017, 2021; A. Botteon et al. 2021; D. N. Hoang et al. 2021).

Radio relics are relatively rare, with about 10% of Planck galaxy clusters hosting at least one relic (e.g., A. Jones et al. 2023). Some merging clusters host double-radio relics, i.e., relics located symmetrically with respect to the cluster center (e.g., A. Bonafede et al. 2014; F. de Gasperin et al. 2014; R. J. van Weeren et al. 2019; A. Jones et al. 2023), of which fewer than 30 confirmed examples are known to date (A. Stroe et al. 2025). There are a handful of clusters with double relics that also host a radio halo, for example, CIZA J2242.8+5301 (R. J. van Weeren et al. 2010; A. Stroe et al. 2013; D. N. Hoang et al. 2017; G. Di Gennaro et al. 2018), PLCK G287.0+32.9 (A. Bonafede et al. 2014; C. Stuardi et al. 2022), PSZ1 G108.18–11.53 (F. de Gasperin et al. 2015), and RXC J1314.4−2515 (C. Stuardi et al. 2019; K. Knowles et al. 2022). The detection rate of radio relics is impacted by the detailed physics of relic formation, compounded by the sensitivity constraints relevant at low surface brightness. Producing double relics requires very particular physical conditions. After the dark matter (DM) core passage in a binary, head-on collision of two clusters, two merger-induced shocks propagate in opposite directions along the merger axis (e.g., S. W. Skillman et al. 2011; R. J. van Weeren et al. 2011a; W. Lee et al. 2024). However, the relics will only "light up" in the radio at relatively large clustercentric distances. The radio emission peaks 1–1.5 Gyr after core passage (e.g., J. Donnert et al. 2016b): this is governed by the kinetic energy dissipated into shocks, which peaks at about $0.5R_{\rm vir}$, and the cosmic-ray (CR) production, which peaks at about 1 Gyr after core passage (F. Vazza et al. 2012; J.-H. Ha et al. 2018). When multiwavelength observation data are available, the merger scenario of double-relic clusters can be well constrained by piecing together information on the gas distribution, location of the shocks, etc. (e.g., K. Roettiger et al. 1999; W. A. Dawson 2013; K. Y. Ng et al. 2015; W. Lee et al. 2020; J. Kim et al. 2021; H. Cho et al. 2022; R. P. Albuquerque et al. 2024). Therefore, double-radio relic clusters offer the unique opportunity to pose tight constraints on particle acceleration mechanisms within the context of a well-understood merger scenario. Comparing clusters with double relics and with/without halos provides the ideal test bed for constraining the cluster properties that govern the formation of radio halos during mergers (M. J. Jee et al. 2016; A. Bonafede et al. 2017; N. Golovich et al. 2019; X. Zhang et al. 2020).

Although only a few more than two dozen double relics are currently known, there could potentially be many more awaiting discovery in the era of large radio surveys (e.g., S. E. Nuza et al. 2017). Instruments such as the LOw-Frequency ARray (LOFAR; M. P. van Haarlem et al. 2013), the upgraded Giant Metrewave Radio Telescope (uGMRT; Y. Gupta et al. 2017), and Square Kilometer Array precursors such as MeerKAT (J. Jonas & MeerKAT Team 2016), with their combination of 5″ resolution, high sensitivity, and intermediate and low radio frequency capabilities uniquely suited to detecting steep-spectrum radio sources, coupled with a large field of view, are already changing the way we study diffuse radio sources in clusters. With these instruments, complex, diffuse radio sources are being discovered in a new parameter space, covering lower masses and higher redshifts than was possible before with shallower surveys at lower resolution (e.g., V. Parekh et al. 2020; G. Di Gennaro et al. 2021; A. Botteon et al. 2022; K. Knowles et al. 2022; W. Lee et al. 2022; S. Chatterjee et al. 2024; S. P. Sikhosana et al. 2024).

2. PSZ2 G181.06+48.47

A spectacular example of a double-relic system is PSZ2 G181.06+48.47 and its associated Mpc-wide diffuse sources (Figure 1). The cluster was originally discovered through the red sequence method in the Sloan Digital Sky Survey (SDSS; B. P. Koester et al. 2007) and was later confirmed through the redMaPPer algorithm (E. S. Rykoff et al. 2014) and through its Sunyaev-Zel'dovich (SZ) effect by Planck (Planck Collaboration et al. 2016). More recently, spectroscopy in the region of the source from SDSS Data Release 18 (DR18; A. Almeida et al. 2023) confirms the presence of an overdensity of galaxies at $z \sim 0.234$ (A. Stroe et al. 2025).

As a relatively low mass cluster ($M_{\rm SZ} = 4.2^{+0.5}_{-0.5} \times 10^{14}\, M_{\odot}$, Planck Collaboration et al. 2016; weak lensing $M_{500,\rm WL} = 2.9^{+0.75}_{-0.69} \times 10^{14}\, M_{\odot}$, E. Ahn et al. 2025; X-ray $M_{500,\rm X} = 2.57^{+0.37}_{-0.38} \times 10^{14}\, M_{\odot}$, A. Stroe et al. 2025) at $z = 0.234$, and seemingly devoid of any particularly interesting features, PSZ2 G181.06+48.47 initially eluded further study. A recent X-ray study suggests that this cluster is one of the most disturbed clusters in the Planck sample, exhibiting a complex morphological and thermodynamic structure (A. Stroe et al. 2025).

The redshift and mass of the cluster and the sizes and luminosities of the diffuse sources place them within the reach of deep, pointed, state-of-the-art observations but below the limits of classical radio survey detection limits. The twin sources were detected in the recent LOFAR 144 MHz observation thanks to the unique combination of observing frequency, sensitivity, and resolution (T. W. Shimwell et al. 2019; A. Botteon et al. 2022). With otherwise typical radio powers and sizes, the two putative relics are located exceptionally far (>1.2 Mpc) away from the putative cluster core, beyond $R_{500} \sim 0.93$ Mpc close to $R_{200} \sim 1.43$ Mpc, given the low mass of the host cluster (E. Ahn et al. 2025; A. Stroe et al. 2025).

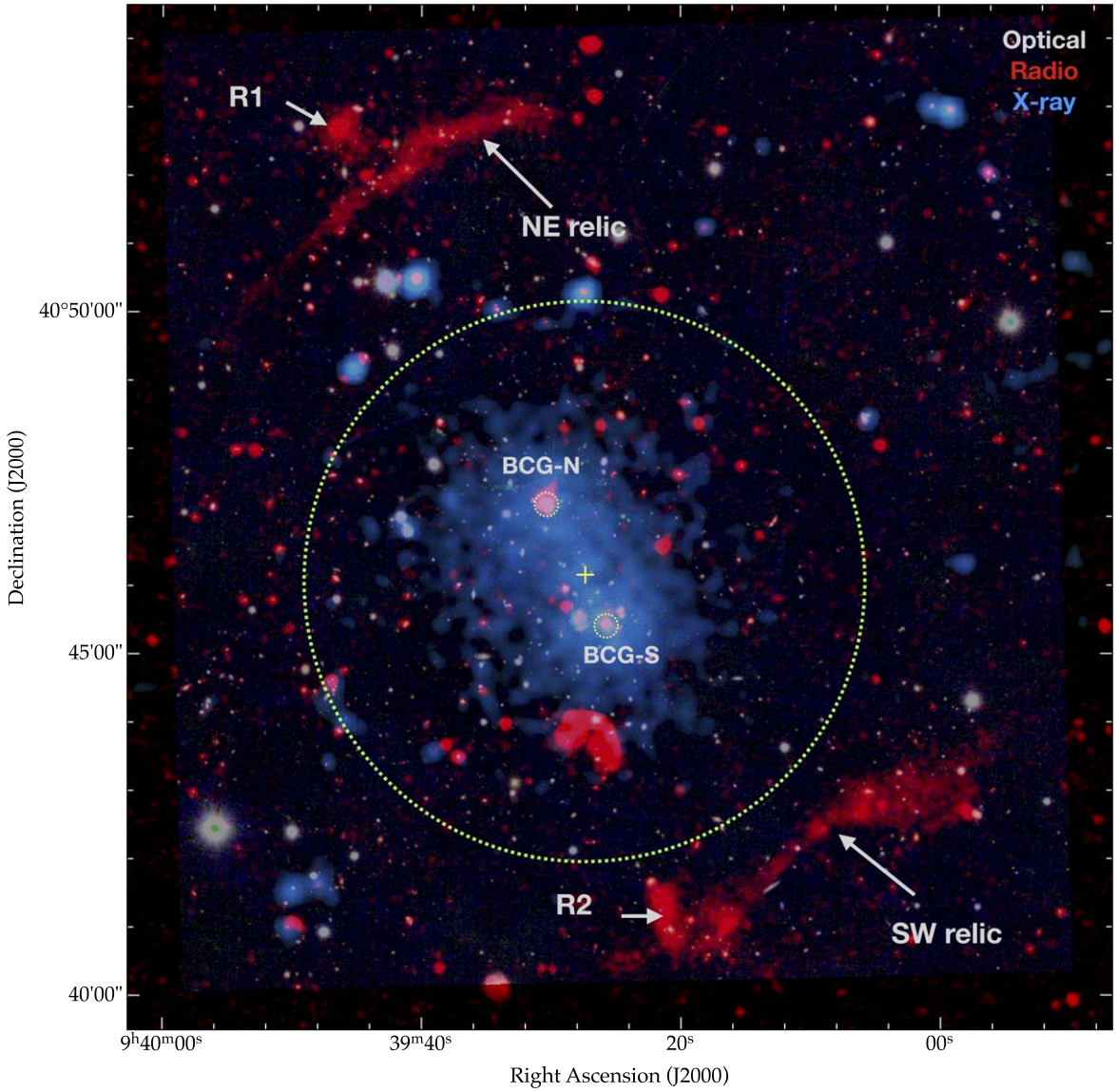

Figure 1. Radio, X-ray, and optical overlay of PSZ2 G181.06+48.47, a post-core-passage merging cluster system. The radio emission from LOFAR (144 MHz; A. Botteon et al. 2022) and uGMRT Band 3 (380 MHz) is shown in red, while blue traces the 0.5–2.0 keV XMM-Newton X-ray emission (A. Stroe et al. 2025). In the background, the color-composite red, green, and blue optical image was created using Pan-STARRS *g*, *r*, and *i* data. The yellow plus sign marks the center of the system. We label the most prominent diffuse radio sources (R2 is a radio galaxy; R1 is a diffuse source) and mark the two brightest cluster galaxies, strong radio point sources, with dotted circles. The green circle represents R_{500} of the cluster.

The bright diffuse sources located in a low-mass cluster at such large clustercentric distances, where the plasma density is low, can place valuable tests on relic formation models. Are the relics associated with particularly strong shocks? Is the CR density higher than expected? Could a more complex cluster merger history explain the morphology and location of the two diffuse sources?

To leverage the unique insights PSZ2 G181.06+48.47 offers into particle acceleration in low-mass clusters, we began a multiwavelength observational campaign to unveil the thermal and nonthermal cluster properties in the context of its merger history. In the present paper, we focus on unveiling the nature, physics, and formation mechanisms of the diffuse radio sources associated with the cluster through broadband radio observations spanning from 120 MHz to 1.5 GHz. Through a detailed analysis of the thermodynamic properties of the ICM, A. Stroe et al. (2025) characterize the subclusters, identify merger-associated discontinuities, and pose constraints on the merger history, while E. Ahn et al. (2025) focus on a weak-lensing (WL) analysis of the cluster aimed at understanding the mass properties of the clusters and its merger history and, more broadly, constraining DM properties.

This paper is structured as follows: In Section 3, we introduce the new VLA and uGMRT observations, present our data reduction strategy, and list ancillary data. Section 4 describes the total intensity, spectral, and polarization analysis techniques employed in exploring the data. In Section 5 we present the results of our analysis, including morphological, integrated, and resolved spectral, color–color, and polarimetric properties of the sources. In Section 6, we investigate the origin of the diffuse radio sources in the context of the merger scenario that best fits PSZ2 G181.06+48.47. Concluding remarks can be found in Section 7. Throughout this paper, we adopt a flat ΛCDM cosmology with $H_0 = 69.6\,\mathrm{km\,s^{-1}\,Mpc^{-1}}$, $\Omega_m = 0.286$, and $\Omega_\Lambda = 0.714$ (E. L. Wright 2006). At the cluster redshift of $z = 0.234$, $1''$ corresponds to a physical scale of 3.753 kpc. We

Table 1
Overview of VLA, uGMRT, and LOFAR Observations

	VLA L Band			uGMRT		LOFAR HBA[a]
	B Configuration	C Configuration	D Configuration	Band 4	Band 3	
Frequency range	1–2 GHz	1–2 GHz	1–2 GHz	550–850 MHz	300–500 MHz	120–168 MHz
Channel width	1 MHz	1 MHz	1 MHz	48.8 kHz	130 kHz	12.2 kHz
Correlations	full Stokes	full Stokes	full Stokes	RR and LL	RR and LL	full Stokes
On-source time	4 hr	2 hr	2 hr	9 hr	9 hr	8 hr

Note. VLA observations were recorded in 16 spectral windows (64 channels in each spectral window).
[a] Observation presented in A. Botteon et al. (2022).

Table 2
Imaging Properties of Radio Maps Used in the Analysis

	Name	Restoring Beam	Robust Parameter	*u-v* Cut	*u-v* Taper	rms Noise (μJy beam^{-1})
LOFAR HBA (120–169 MHz)	IM1	$8\farcs1 \times 5\farcs3$	−0.5	⋯	⋯	70
	IM2	$20'' \times 20''$	−0.5	⋯	15″	200
	IM3	$20'' \times 20''$	−0.5	$\geqslant$0.15 $k\lambda$	15″	210
uGMRT Band 3 (300–500 MHz)	IM4	$6\farcs8 \times 5\farcs6$	0.0	⋯	⋯	15
	IM5	$20'' \times 20''$	0.0	⋯	12″	42
	IM6	$20'' \times 20''$	−0.5	$\geqslant$0.15 $k\lambda$	15″	65
	IM7	$25'' \times 25''$	0.0	⋯	25″	90
uGMRT Band 4 (550–850 MHz)	IM8	$5'' \times 5''$	0.0	⋯	⋯	10
	IM9	$20'' \times 20''$	0.0	⋯	12″	22
	IM10	$20'' \times 20''$	−0.5	$\geqslant$0.15 $k\lambda$	15″	25
VLA *L*-band (1–2 GHz)	IM11	$8\farcs5 \times 7\farcs4$	0.0	⋯	⋯	9
	IM11	$20'' \times 20''$	0.0	⋯	15″	14
	IM13	$20'' \times 20''$	−0.5	$\geqslant$0.15 $k\lambda$	15″	17

Note. Imaging was performed in `WSCLEAN` using `multiscale` and with the `Briggs` weighting scheme.

use a cluster center defined to sit between the two subclusters at R.A. = 144.°866 and decl. = 40.°774 (A. Stroe et al. 2025).

3. Observations and Data Reduction

3.1. Very Large Array

The cluster was observed with the Karl G. Jansky Very Large Array (VLA) using the L band (1–2 GHz) in the B, C, and D configurations (project code: SL0429; PI: A. Stroe; see Table 1). For each configuration, 3C 286 was included as a flux calibrator, observed for 6 minutes at the start of the observation. One of two radio sources (J0832+4913 or J1006+3454) was included as a phase calibrator.

The data were calibrated and imaged with the Common Astronomy Software Applications (`CASA`; J. P. McMullin et al. 2007; CASA Team et al. 2022) package. Data obtained from different observing runs were calibrated separately but in the same manner. The data were Hanning smoothed and inspected for radio frequency interference (RFI), and the affected data were flagged using the `tfcrop` mode from the `flagdata` task. Low-amplitude RFI was flagged using `AOFlagger` (A. R. Offringa et al. 2010). Following flagging, we determined and applied elevation-dependent gain tables and antenna offset positions. To prevent the flagging of good data due to the bandpass roll-off at the edges of the spectral windows, we corrected for the bandpass using the calibrator 3C 48. We used the L-band 3C 137 and 3C 286 models provided by the `CASA` software package and set the flux density scale according to R. A. Perley & B. J. Butler (2013). An initial phase calibration was performed using both calibrators over a few channels per spectral window. We then corrected the antenna delays and determined the bandpass response using the calibrator 3C 147. Applying the bandpass and delay solutions, we proceeded with the gain calibration.

Following initial calibration and flagging, several rounds of self-calibration were performed to refine the calibration for each individual data set. We imaged the data in CASA with the W-projection algorithm (T. J. Cornwell et al. 2008). Clean masks made using the `PyBDSF` source detection package (N. Mohan & D. Rafferty 2015) were employed for each imaging step. The spectral index and curvature were taken into account during deconvolution using nterms = 2 (U. Rau & T. J. Cornwell 2011). After self-calibration, the B, C, and D configuration data were combined, achieving denser *u-v* coverage. Final imaging of the combined data sets (BCD configurations) was completed in `WSClean` (A. R. Offringa et al. 2014), using Briggs weighting and employing the wideband and multiscale algorithms (A. R. Offringa & O. Smirnov 2017). The resulting images, providing an optimal balance between resolution and noise levels, were corrected for the primary beam attenuation in WSClean. The detailed parameters for the images are listed in Table 2.

3.2. uGMRT

PSZ2 G181.06+48.47 was observed with the uGMRT in Band 4 and Band 3 (project code 38_062; PI: A. Stroe) using the GMRT Wideband Backend (GWB). The observations were

conducted in multiple observing runs between 2020 September and 2021 January, with 3C 147 and 3C 286 included as flux calibrators. We summarize the observational details in Table 1.

The uGMRT data were processed using Source Peeling and Atmospheric Modeling (H. T. Intema et al. 2009), which includes both direction-independent and direction-dependent calibration. The flux densities of the primary calibrator were set according to A. M. M. Scaife & G. H. Heald (2012). Following flux density scale calibration, the data were averaged, flagged, and corrected for the bandpass. The phase gains were corrected with a global sky model obtained with the GMRT narrowband data. The calibrated subbands were combined to produce deep, full-continuum images. The final deconvolution was performed in WSClean using multiscale and Briggs weighting with robust parameter 0 (see Table 2) and corrected for primary beam.

3.3. LOFAR

The cluster was observed with LOFAR High Band Antenna (HBA) dual inner mode as part of the LOFAR Two-meter Sky Survey. Our analysis uses the calibrated data and the images released as part of the LOFAR DR2 (see Table 2 and T. W. Shimwell et al. 2019). For a detailed description of the observation and data reduction, we refer to A. Botteon et al. (2022).

3.4. Ancillary Observations

To aid in the interpretation of the radio data, we also employ multiwavelength observations compiled through the Vizier database (F. Ochsenbein et al. 2000), including optical spectroscopy from SDSS DR18 (A. Almeida et al. 2023). We also make use of data from the first data release from the Panoramic Survey Telescope and Rapid Response System (Pan-STARRS; H. A. Flewelling et al. 2020) and new, targeted Chandra and XMM-Newton X-ray observations (A. Stroe et al. 2025).

4. Spectral and Polarization Analysis Techniques

We describe below the radio, spectral index, and polarization maps we produced to investigate the morphological, spectral, and polarimetric properties of the radio sources in PSZ2 G181.06+48.47.

4.1. Radio Stokes I Maps

We label the most prominent sources in Figure 1, while in Figure 2 we show high-resolution radio images of the cluster. To highlight radio emission on a range of spatial scales of interest, we also prepared a set of medium-resolution (20″) images shown in Figure 3. These maps are created without any *u-v* cut. High-resolution zoom-in maps on the most prominent patches of diffuse emission are shown in the left panels of Figures 4 and 5. For image properties, see Table 2.

Additionally, to identify the lowest surface brightness radio features in the cluster, we also created our lowest-resolution (25″) uGMRT Band 3 image using `robust = 0.5` and *u-v* tapering (discussed in Section 6.5).

4.2. Spectral Analysis

To examine the spectral characteristics of the diffuse radio sources in the PSZ2 G181.06+48.47 field across a broad frequency range, we combined our uGMRT Band 3 (300–500 MHz), Band 4 (550–850 MHz), and VLA (1–2 GHz) observations with the published LOFAR HBA (120–169 MHz) observations (A. Botteon et al. 2022). To ensure consistency in the flux density distribution at all observed frequencies obtained from different radio interferometric telescopes, it is crucial that all images reflect structures over the same range of angular scales (e.g., A. Stroe et al. 2016; K. Rajpurohit et al. 2020a). Therefore, we imaged the radio data using a Briggs weighting scheme (`robust = -0.5`), *u-v* tapering, and a common lower *u-v* cut at 0.15kλ, the shortest, well-sampled baseline of the uGMRT data. This *u-v* cut was applied to the VLA L-band and LOFAR data. For spectral analysis, we created a set of images with different resolutions: 20″, 10″, and 7″. The 20″ resolution was chosen to properly exclude the contamination from unrelated sources, while allowing the recovery of diffuse flux from low surface brightness regions. The high-resolution maps (10″ and 7″) enable us to capture fine spectral index details and trends across both relics.

The flux density scale of all observations (LOFAR, uGMRT, and VLA) was confirmed by comparing the spectra of compact sources between 144 MHz and 1.5 GHz. The uncertainty in the flux density measurements was estimated as

$$\Delta S = \sqrt{(f \cdot S)^2 + N_{\rm beams} \quad (\sigma_{\rm rms})^2}\,, \tag{1}$$

where f is the absolute flux density calibration uncertainty, S is the flux density, $\sigma_{\rm rms}$ is the rms noise, and $N_{\rm beams}$ is the number of beams. We assumed absolute flux density uncertainties of 10% for LOFAR HBA (T. W. Shimwell et al. 2022), uGMRT Band 3, and uGMRT Band 4 (P. Chandra et al. 2004) and 4% for the VLA L-band data (R. A. Perley & B. J. Butler 2013).

The high-resolution spectral index maps of the NE and SW relics, between 144 and 380 MHz, are shown in the right panels of Figures 4 and 5. Pixels below $3\sigma_{\rm rms}$ were blanked at both frequencies. For the purpose of measuring integrated spectral indices, we used the 20″-resolution images. The specific regions from which flux densities were extracted are indicated in the right panel of Figure 6, where point sources were masked.

The medium-resolution spatially resolved spectral index maps, created between 144 and 380 MHz and between 144 MHz and 1.5 GHz, are shown in Figure 7. Pixels were excluded if the flux density at both frequencies is below $3\sigma_{\rm rms}$.

4.3. Color–Color Plots

Radio color–color plots, in which the spectral index at low frequencies is plotted against the spectral index at high frequencies, are a powerful tool for analyzing the spectral properties of radio sources and for identifying overlapping regions (D. M. Katz-Stone et al. 1993; D. M. Katz-Stone & L. Rudnick 1997; R. J. van Weeren et al. 2011b; A. Stroe et al. 2013; K. Rajpurohit et al. 2020a; K. Rajpurohit et al. 2022b). The low-frequency spectral index is estimated between 144 and 380 MHz, while the high frequency is between 700 MHz and 1.5 GHz. In Figure 8, we show the color–color plot obtained for the diffuse sources in PSZ2 G181.06+48.47. Points that fall on the unity line ($\alpha^{380\ \rm MHz}_{144\ \rm MHz} = \alpha^{1.5\ \rm GHz}_{700\ \rm MHz}$) indicate a simple power-law spectrum, where the spectral index remains constant across frequencies. Any deviations from the power line imply negative (convex) or positive (concave) curvature. According to the spectral index convention we use, the curvature is negative for a convex spectrum.

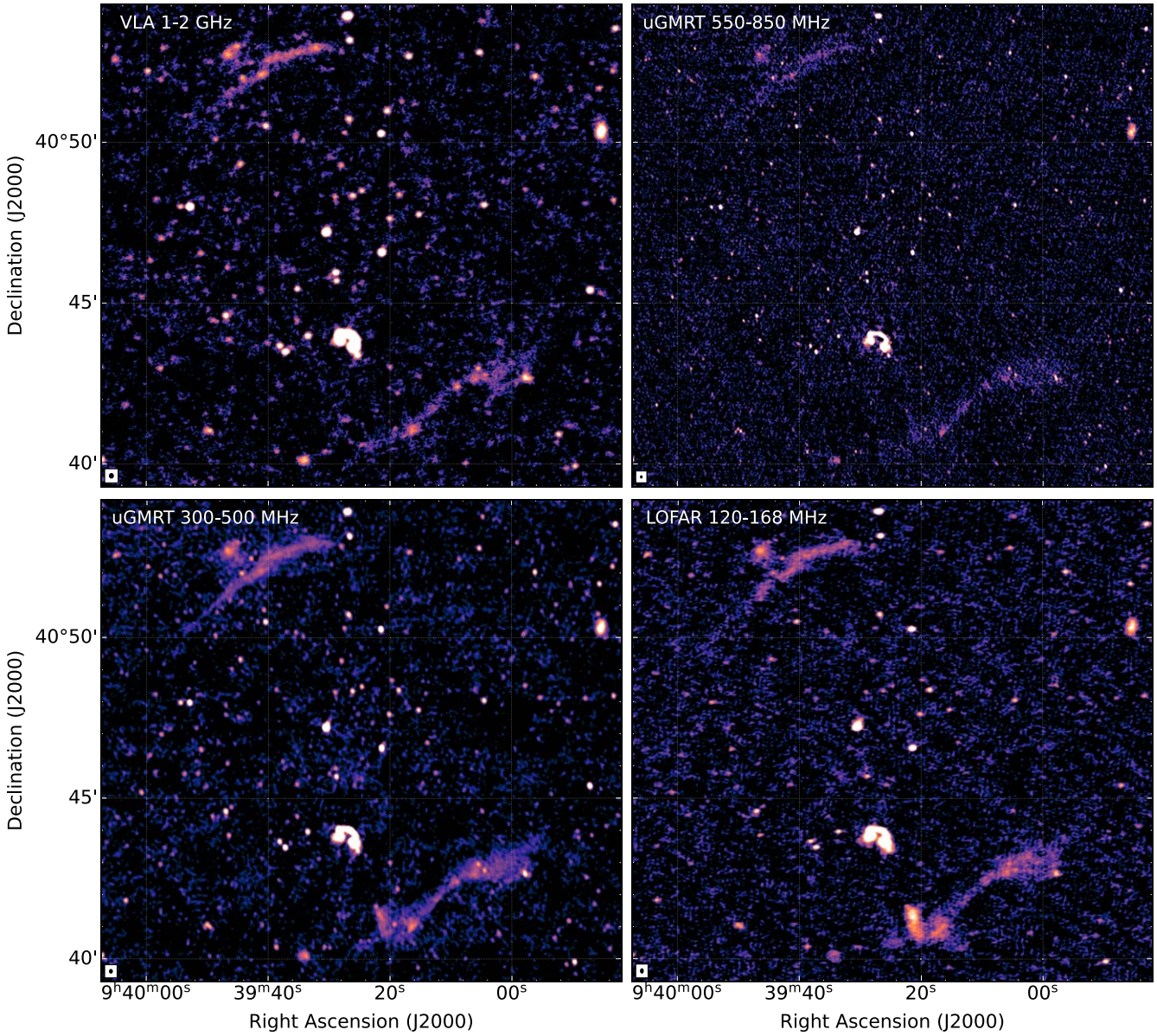

Figure 2. High-resolution VLA L-band (top left), uGMRT Band 4 (top right), uGMRT Band 3 (bottom left), and LOFAR HBA (bottom right) images of PSZ2 G181.06+48.47 in square-root scale. The beam size is indicated in the lower left corner of each panel. Detailed image parameters are listed in Table 2.

4.4. Polarization Analysis

VLA L-band (1–2 GHz) images of the Stokes *I*, *Q*, and *U* were obtained with `CASA`, employing `robust` = 0.5 weighting and a *u-v* taper of 15″. The Stokes cubes affected by artifacts or exhibiting a high level of noise were excluded from the analysis. A total of 42 Stokes *IQUV* cubes were used for the whole 1–2 GHz band. As the output Stokes cubes have slightly different resolutions, all Stokes cubes were convolved to a common restoring beam of 25″. Since the diffuse sources of interest exhibit low surface brightness, this resolution allows us to get a high signal-to-noise ratio and recover low surface brightness emission. Each image was corrected for the primary beam.

We performed rotation measure (RM) synthesis (RM-synthesis; M. A. Brentjens & A. G. de Bruyn 2005) on the Stokes *IQUV* cubes using the `pyrmsynth`[14] code. The RM cube was created between $\pm 300\,\mathrm{rad\,m^{-2}}$ with a bin size of $5\,\mathrm{rad\,m^{-2}}$. Since the first sidelobes of the RM spread function were significant, we cleaned down to five times the noise level of full-bandwidth *Q* and *U* images using the `RM-CLEAN` algorithm. We used a polarization intensity (*P*) image at a central frequency of 1.5 GHz generated by the `pyrmsynth` code to create a fractional polarization map via

$$\Pi = P/I, \tag{2}$$

where *I* is the Stokes *I* image at 1.5 GHz. The polarization angle is then calculated using

$$\chi = 0.5 \arctan\left(\frac{U}{Q}\right). \tag{3}$$

Polarization intensity maps with overlaid magnetic field vectors focusing on the NE and SW regions are shown in Figure 9, while the resulting RM map is shown in Figure 10. The measured polarization fraction of diffuse sources is summarized in Table 3.

[14] https://github.com/mrbell/pyrmsynth

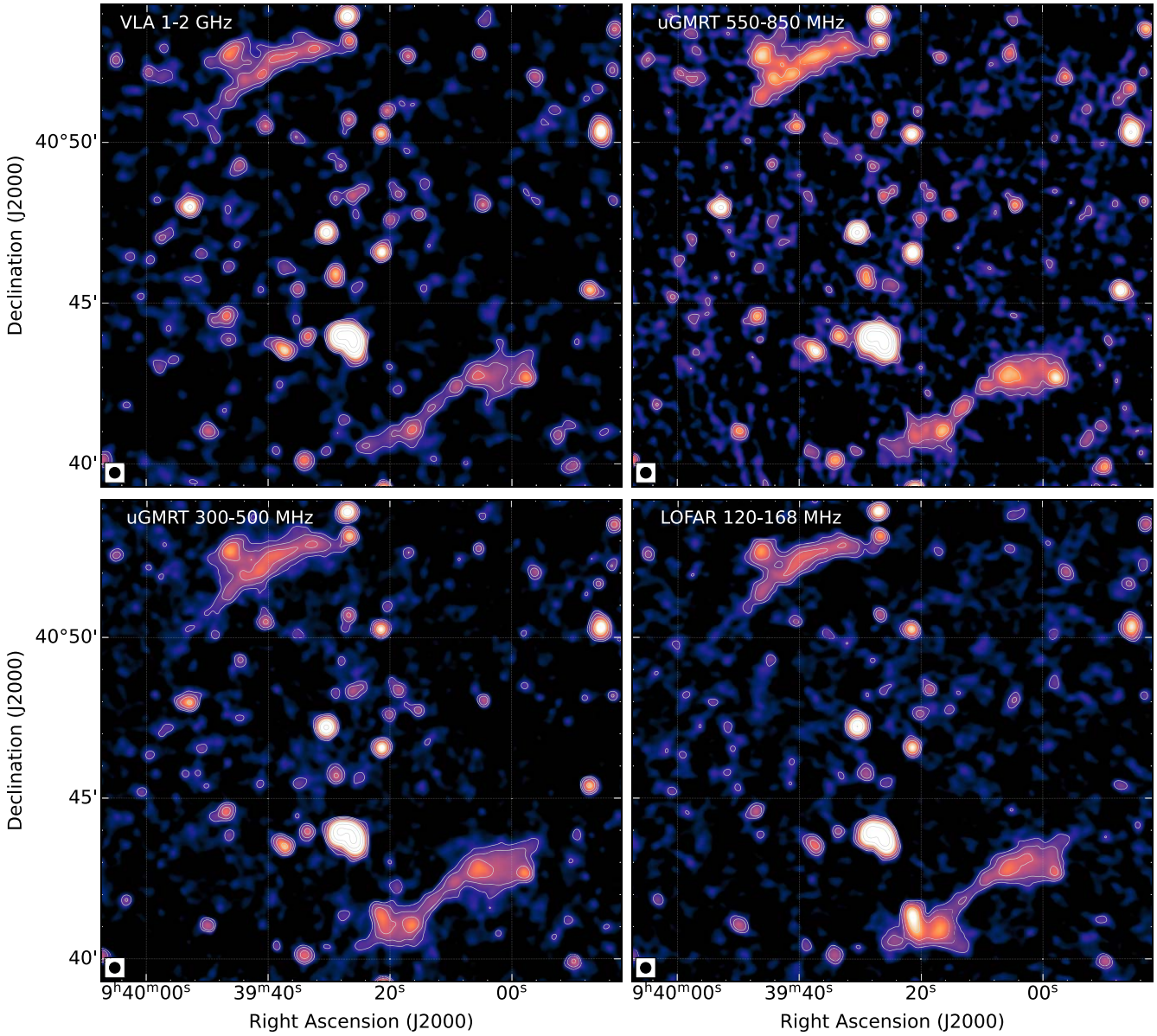

Figure 3. Low-resolution VLA *L*-band (top left), uGMRT Band 4 (top right), uGMRT Band 3 (bottom left), and LOFAR HBA (bottom right) images of the PSZ2 G181.06+48.47 cluster. All images have a common resolution of 20″. The beam size is indicated in the lower left corner of each panel.

5. Results

We investigate a number of diffuse sources in the cluster, whose properties are summarized in Table 4.

5.1. Radio Morphologies

Two large diffuse sources located on the northeast and southwest periphery of the cluster (NE and SW) are detected across 1.2 dex in frequency, from 120 MHz to 2 GHz (Figures 2 and 3). Measured from center to center, their projected relative distance is ∼2.6 Mpc.

With a largest linear size (LLS) of ∼1.2 Mpc at 144 MHz and a very thin (∼70 kpc) morphology toward its northeastern end, the NE source appears to consist of two filaments, in particular at 1.5 GHz (Figure 2). The source is located about 1.35 Mpc from the system center. The sensitive high-resolution images allow us to identify at least seven compact sources with optical counterparts embedded in NE, with the one source with a spectroscopic redshift ($z_{\rm spec} = 0.499584$) confirmed as not a cluster member. We present a point-source-subtracted high-resolution Band 3 image of the NE source in Figure 4. The diffuse (LLS = 370 kpc at 144 MHz) source R1 is connected to NE via a faint, 125 kpc wide bridge of emission.

Source SW, located ∼1.18 Mpc away from the cluster center, has a nonuniform brightness across its 1.3 Mpc extension (at 144 MHz), which peaks toward the west with a downstream width of about 420 kpc at 144 MHz and 280 kpc at 1.5 GHz (Figure 3). At the center, the source is much thinner, with a width of ∼90 kpc. We identify five embedded compact sources, none of which have spectroscopic redshift measurements (see Figure 5). At SW's eastern end, we detect a blob of bright tailed emission (R2). While R2 appears connected to the eastern end of SW, R2 extends farther to the east. The uGMRT Band 4 high-resolution image separates the source into a compact core and a faint, extended tail (Figure 2). The core is only marginally detected at 1.5 GHz, suggesting a steep

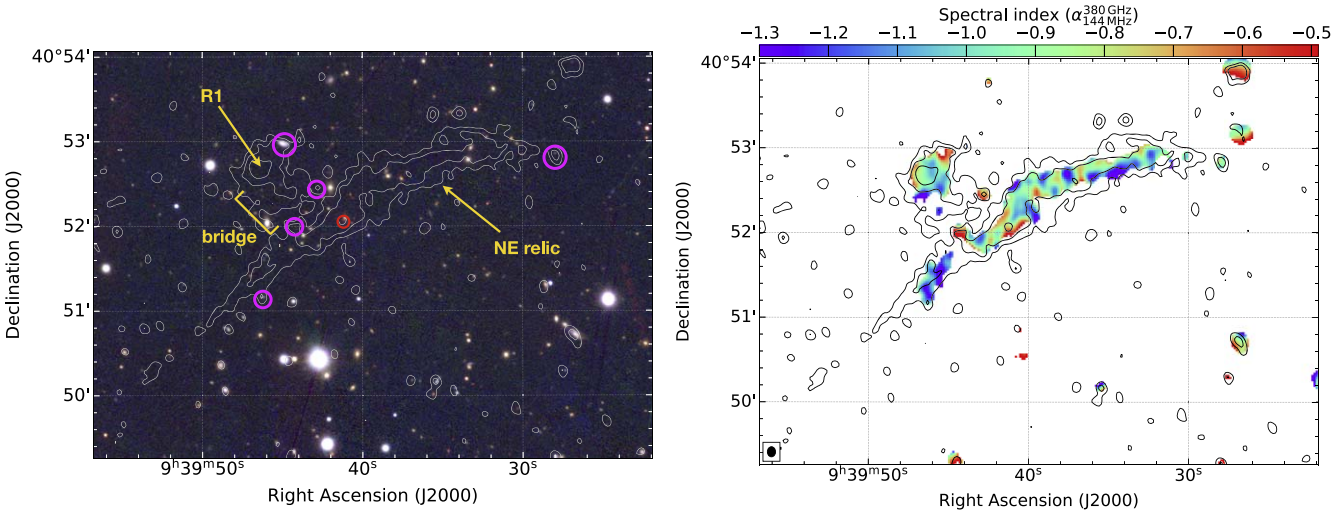

Figure 4. Left: Pan-STARRS image overlaid with a uGMRT Band 4 high-resolution ($7'' \times 6''$) point-source-subtracted image of the NE relic. The beam size is indicated in the lower left corner of each panel. Contours are drawn at [1, 2, 4, 8. . .] $\times$ $3.0\sigma_{\rm rms}$. The discrete sources subtracted from the u-v data are marked with circles, with only one having an available redshift (red circle). Right: $10''$-resolution spectral index map (144–380 MHz) of the NE relic, with uGMRT Band 3 contours drawn at [1, 2, 4, 8...] $\times$ 4 $\sigma_{\rm rms}$.

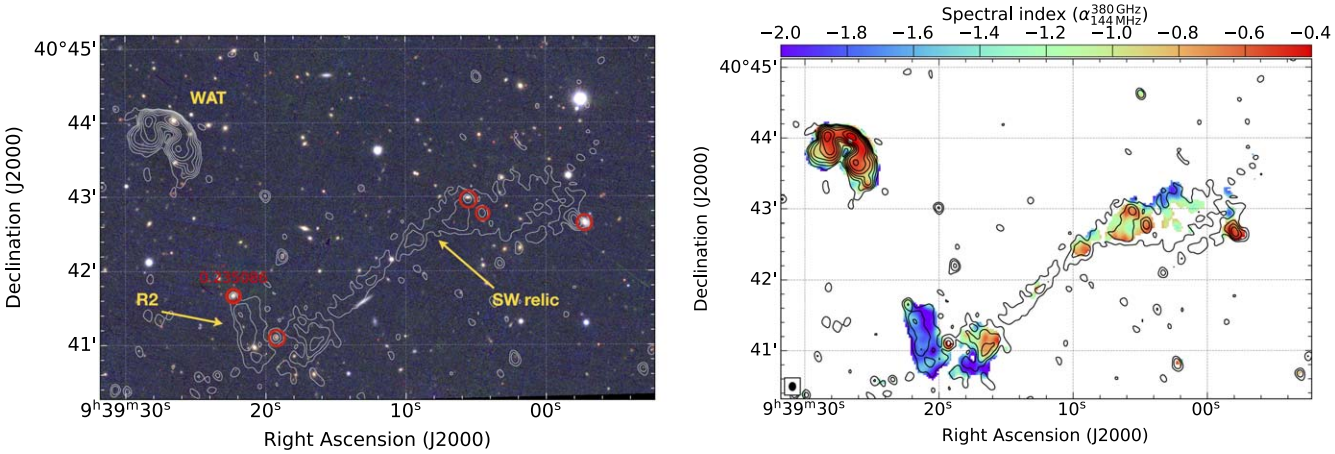

Figure 5. Left: Pan-STARRS zoom-in view of the SW relic overlaid with uGMRT Band 3 $10''$-resolution radio contours. Right: high-resolution ($10''$) spectral index map of the SW relic between 144 and 380 MHz. The uGMRT Band 3 Stokes I contours are plotted at [1, 2, 4, 8, ...] $\times 3\ \sigma_{\rm rms}$, where $\sigma_{\rm rms} = 18\ \mu$Jy beam^{-1}.

spectrum. A spectroscopically confirmed cluster member ($z_{\rm spec} = 0.235086$) coincides with the compact core emission at the north of R2, as shown in Figure 5 (left panel).

In our lowest-resolution GMRT Band 3 image, we observe a hint of low-significance ($\geqslant 2\sigma$ level) diffuse emission in the central region of the cluster (discussed in Section 6.5). The source is not detected at a similar level in any of the other low-resolution maps, suggesting a steep spectrum.

5.2. Integrated Radio Spectra and Radio Powers

The integrated spectra of NE, SW, R1, and R2 between 144 MHz and 1.5 GHz are shown in the left panel of Figure 6 and summarized in Table 4. Note that the spectral indices are measured after excluding the compact sources with optical counterparts. The integrated spectral indices of NE and SW are $\alpha = -0.92 \pm 0.04$ and $\alpha = -1.09 \pm 0.05$, respectively. The radio emission between NE and SW has a flux density of about 2.1 mJy at 380 MHz, excluding discrete sources (marked in the right panel of Figure 6). It is worth mentioning that the LOFAR image suffers from calibration artifacts in the central region, resulting in negative flux density, thus not allowing us to recover an accurate flux density at 144 MHz.

We obtain the monochromatic radio power as

$$P = 4\pi D_L^2 S_{\nu_i} (1+z)^{-(1+\alpha)}, \quad (4)$$

where D_L is the luminosity distance to the source, α is the spectral index used in the k-correction, and S_{ν_i} is the flux density at 1.5 GHz and 144 MHz. The estimated radio powers for the diffuse sources in the cluster are listed in Table 4. All the diffuse sources are adequately fit with a single power law up to 1.5 GHz without any obvious break.

5.3. Spatially Resolved Spectral Index Maps

We do not observe any clear spectral index gradient across the NW source at either high or low frequencies (see right panel of Figure 4 and Figure 7). We observe instead varying spectral indices across it, mainly varying between -0.55 and -0.9. Similarly, no clear spectral index gradient oriented toward the cluster center is seen in the emission of diffuse source R1.

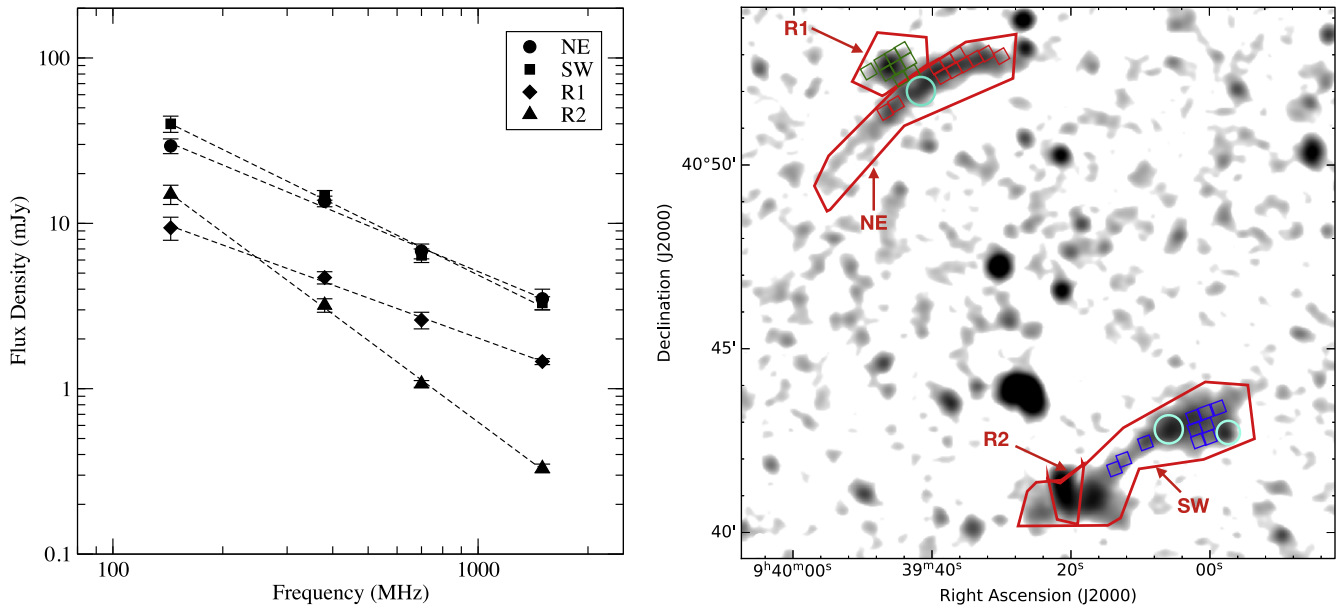

Figure 6. Left: integrated spectra of diffuse radio sources in the PSZ2 G181.06+48.47 cluster from 144 MHz to 1.5 GHz, well described by single power laws (dashed lines). Right: LOFAR 144 MHz image overlaid with regions used for extracting flux densities of NE, SW, R1, and R2. Cyan circles mark masked point sources. Boxes are regions (where emission is detected at all the observed frequencies) used for radio color–color analysis.

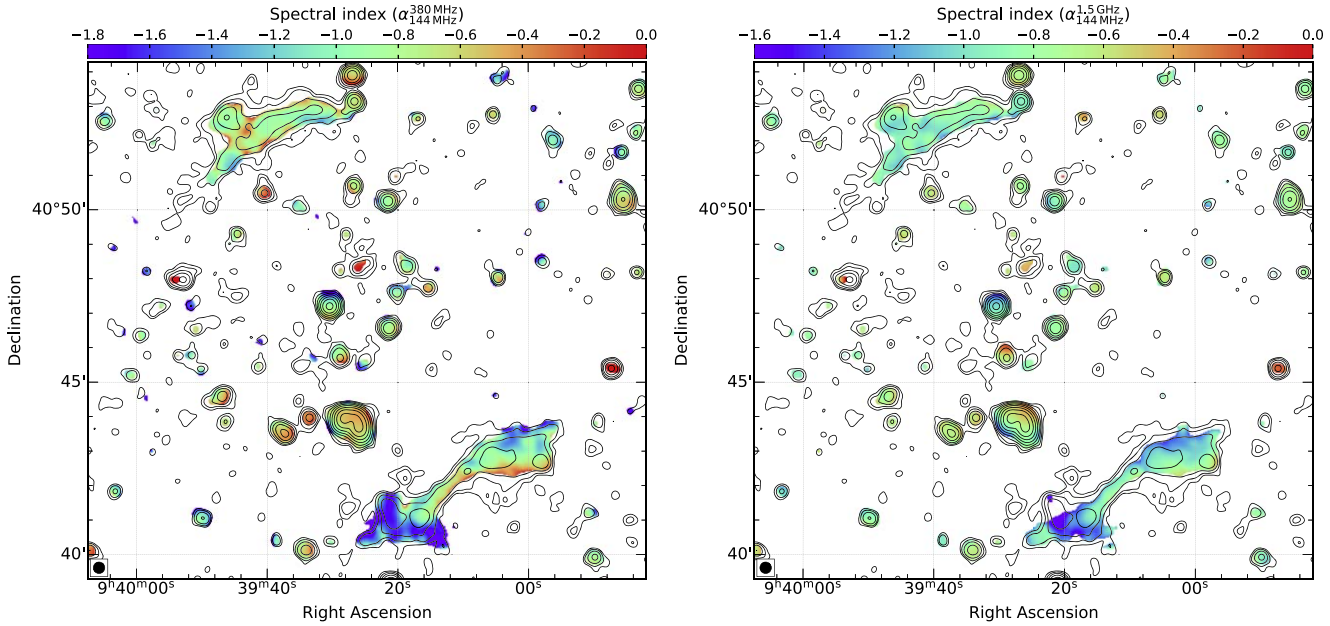

Figure 7. Low- and high-frequency spectral index maps at 20″ resolution: 144 and 380 MHz (left) and 144 MHz and 1.5 GHz (right). Stokes *I* contours from the uGMRT Band 3 *u*-*v*-tapered images are plotted at [1, 2, 4, 8...] ×3 $\sigma_{\rm rms}$, where $\sigma_{\rm rms} = 23$ μJy beam^{-1}.

A noticeable spectral index gradient is observed for the SW source with values varying from −0.6 at the southern leading edge to −1.6 at the northern leading edge; see Figure 7. R2 has distinctly steeper spectral indices compared to the bulk of SW, with the steepest spectral index across R2 reaching −1.8. The high-resolution spectral index map unveils a steep spectral index in the core of R2 (about −1.0), followed by radial steepening in the southwest direction (right panel of Figure 5).

5.4. Polarization Properties

As depicted in Figure 9, the NE source exhibits polarization throughout its entire extent, with the degree of polarization varying between 5% and 42%, with an average of 22%. The magnetic field vectors, after correcting for the Faraday rotation, are aligned with the long axis of the NE source. Unlike NE, R1 is almost completely depolarized at L band.

Some parts of the SW source are polarized, with fractional polarization in the 1%–20% range and an average polarization of 14%, and with magnetic fields aligned with the long axis. R2 is not detected in polarization.

5.5. RM Distribution and Magnetic Field Estimates

The distribution of the peak of RM, the so-called RM map, is shown in Figure 10. The RM spatially varies in the NE source

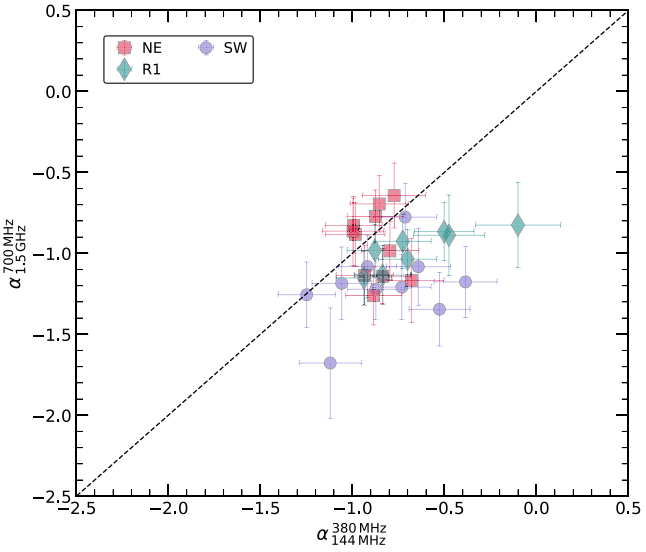

Figure 8. Radio color–color plot of the NE relic, SW relic, and R1, created using the flux densities extracted from 20″ boxes (i.e., the beam size), corresponding to a physical size of about 76 kpc, as shown in the right panel of Figure 6. The dashed line indicates where $\alpha^{380\,\mathrm{MHz}}_{144\,\mathrm{MHz}} = \alpha^{1.5\,\mathrm{GHz}}_{700\,\mathrm{MHz}}$. The three sources display a range of behavior, with only SW showing evidence for spectral aging.

mainly from about +10 to +35 rad m^{-2}, but there are also a few patches with RMs ranging from about +300 to −140 rad m^{-2}. The average $\sigma_{\mathrm{RM}} = 16$ rad m^{-2} across NE suggests very little Faraday-rotating intervening material. For the SW source, we only detect a few patches where the RM is mainly in the range from +6 to +15 rad m^{-2}. Since the expected Galactic RM at the location of the cluster is ∼3 rad m^{-2} (S. Hutschenreuter et al. 2022), the detected RMs slightly deviate from the average Galactic foreground.

Under a simple assumption, the dispersion in RM within the telescope beam, σ_{RM}, can be used to constrain the magnetic field strength (D. D. Sokoloff et al. 1998):

$$\sigma_{\mathrm{RM}} = \sqrt{\frac{1}{3}} \cdot 0.81 \cdot \frac{\langle n_e \rangle}{\mathrm{cm}^{-3}} \cdot \frac{B_{\mathrm{turb}}}{\mu G} \cdot \sqrt{\left(\frac{L}{\mathrm{pc}} \cdot \frac{t}{\mathrm{pc}}\right) \cdot \frac{1}{f}}, \quad (5)$$

where $\langle n_e \rangle$ represents the average thermal electron density of the ionized gas along the line of sight, B_{turb} denotes the magnetic field strength, and f represents the volume filling factor of the Faraday-rotating plasma. L and t refer to the path length through the thermal gas and turbulence scale, respectively.

We use $f = 0.5$ (M. Murgia et al. 2004), $t = 60$ kpc (RM fluctuations), and $\sigma_{\mathrm{RM}} = 16$ rad m^{-2} for the NE relic. We assume a thermal electron density at R_{500} of $n_e = 10^{-4}$ cm^{-3} (the value cannot be measured directly from the data because of the low S/N) and $L \sim 1.5$ Mpc. By inserting all values in Equation (5), we obtain a value of $B = 0.8\,\mu$G for the NE relic. We note that the obtained value depends on the assumed L and the magnetic field value should be seen as a lower limit. The strong depolarization across the SW relic does not allow us to constrain its intrinsic polarization fraction, σ_{RM}, and thus the magnetic fields. However, some detected polarized patches suggest a similar magnetic field value for the SW relic.

6. Discussion

PSZ2 G181.06+48.47 provides an ideal environment in which to test particle acceleration in a low-mass cluster and a low plasma density regime. By bringing together different lines of evidence from both the radio data and the complementary X-ray and WL observations, we aim to obtain a comprehensive understanding of the cluster by exploring the origin of the multitude of diffuse radio sources from the perspective of the cluster merger scenario.

6.1. Diffuse Radio Source Classification

The first step in getting a comprehensive picture of the diffuse emission in the cluster is elucidating the nature and classifying sources NE, SW, R1, and R2.

Based on its location relative to the center of the cluster, its morphology, its high degree of polarization (discussed in Section 6.4), and the absence of clear optical counterparts, we classify NE as a radio relic. The integrated spectrum of the source is in line with other relics, which follow a remarkable power-law distribution over a large frequency range (F. Loi et al. 2021; K. Rajpurohit et al. 2020b; K. Rajpurohit et al. 2022b; M. Murgia et al. 2024). Our estimated radio power for NE (see Table 4) is also in agreement with the radio power versus mass relations of known relics (F. de Gasperin et al. 2014; A. Jones et al. 2023; S. W. Duchesne et al. 2024).

The diffuse, steep-spectrum, large-scale emission in the SW source points toward a relic classification. None of the five embedded compact sources (Figure 5) have spectroscopic redshifts, but there seems to be no direct morphological connection with the relic emission. The SW relic morphology in the high-resolution maps (see Figure 5) is inconsistent with that of a double-lobe radio galaxy: there is no obvious compact core emission bracketed by lobe/plume-like emission, the implied physical size places the source in the rare giant radio galaxy category (P. Dabhade et al. 2020), and no bright, optical host can be identified. The spectral index gradient across the SW (e.g., R. J. van Weeren et al. 2011a; A. Stroe et al. 2013; K. Rajpurohit et al. 2018) supports a relic origin and rules out its classification as a double-lobed radio galaxy. The leading southern edge of the relic is the site of CR electron (CRe) acceleration at the shock front, where we expect the flattest spectral index. In the downstream regions, the spectral index steepens as the shock front propagates outward, which is believed to be due to the aging of electrons because of inverse Compton and synchrotron energy losses (R. J. van Weeren et al. 2010; A. Stroe et al. 2013), or variation of the Mach number across the shock surface (S. W. Skillman et al. 2013). Further, SW's radio power falls confidently within the expected relic scaling relations (F. de Gasperin et al. 2014; A. Jones et al. 2023; A. Stroe et al. 2025). For the PSZ2 G181.06+48.47 relics and other known double relics' radio power versus mass relations, we refer to A. Stroe et al. (2025).

Despite their clear connection, the observations strongly suggest a different nature for R2 compared to SW. R2's morphology resembles a tailed radio galaxy, in particular at 144 and 380 MHz. Moreover, the spectral index of −1.0 at R2's core is much steeper than values typically detected in the core of radio galaxies (mostly in the range of −0.5 to −0.7; A. Stroe et al. 2013; A. Botteon et al. 2020), which seems consistent with an old tailed radio galaxy.

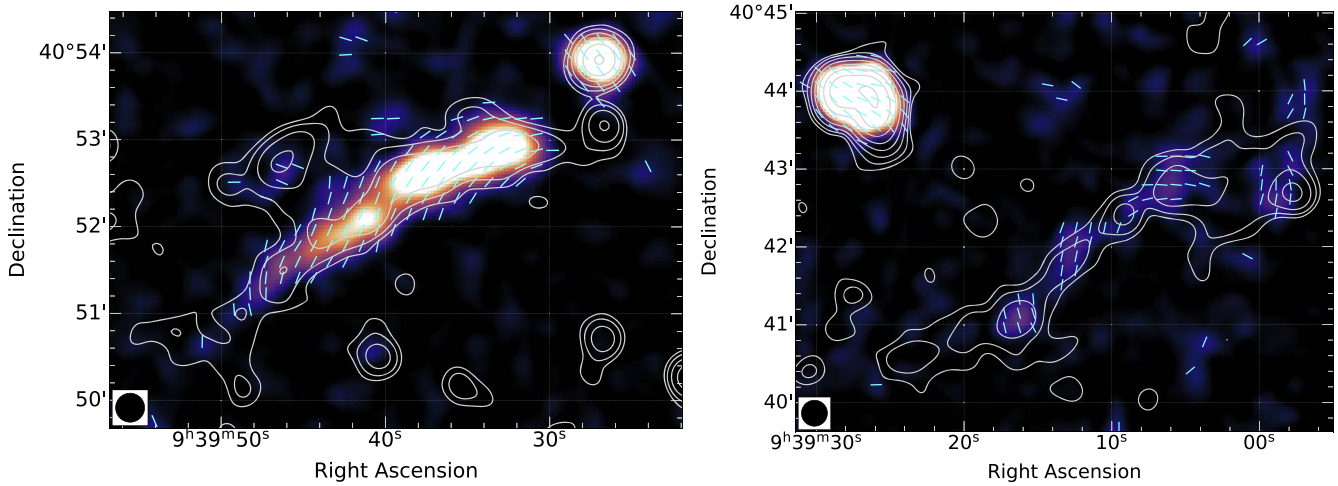

Figure 9. Polarization intensity maps of the NE (left) and SW (right) relics overlaid with magnetic field vectors. Their orientation represents the projected magnetic field corrected for the contribution from the Galactic foreground. Stokes *I* contours from the 1.5 GHz VLA image are drawn at [1, 2, 4, 8. . .] × $5\sigma_{\rm rms}$. The two relics are very differently polarized.

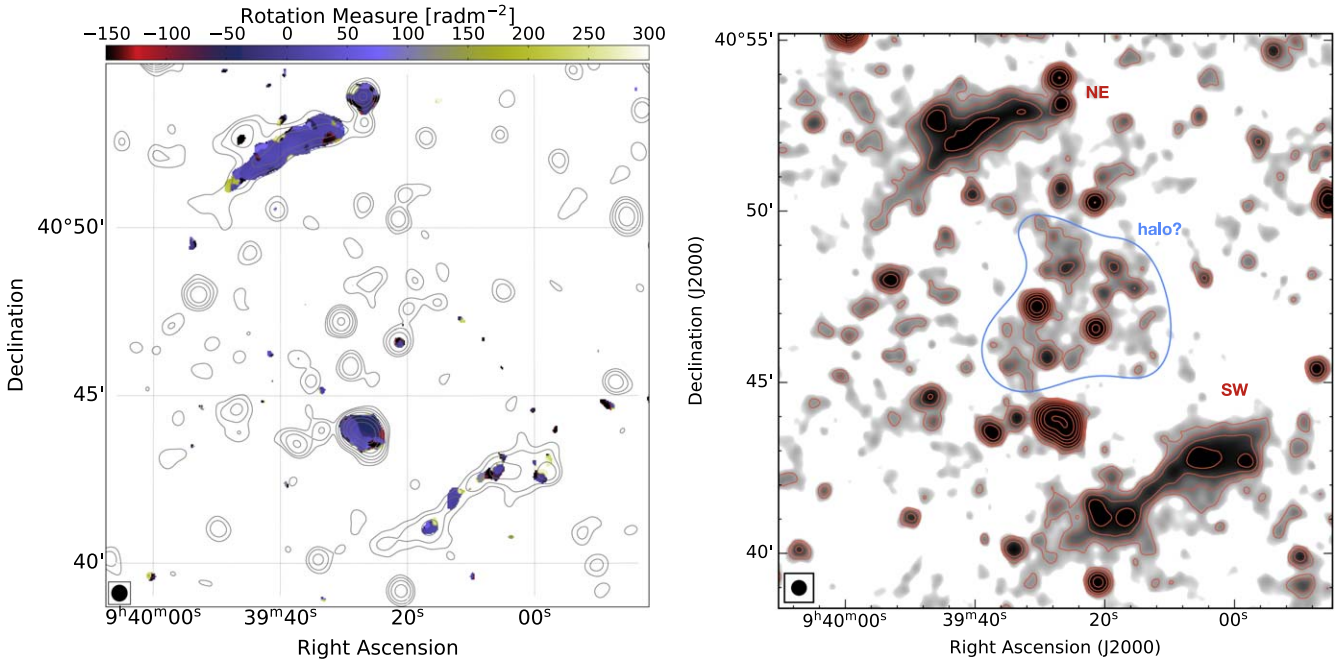

Figure 10. Left: RM map measured over 1.0–2.0 GHz using the RM-synthesis technique. The beam size is 25″. The map is corrected for the Ricean bias. Right: uGMRT Band 3 total intensity image of the cluster at 25″ resolution. Red contours are drawn at [1, 2, 4, 8, ...] ×3 $\sigma_{\rm rms}$, where $\sigma_{\rm rms} = 40$ μJy beam^{-1}, and from the uGMRT Band 3 image (25″ resolution). The candidate radio halo is marked in blue.

Table 3
Diffuse Radio Source Properties

Source	Classif.	Avg. Pol. Frac.	Max. Pol. Frac.	$\mathcal{M}_{\rm R}$	$\mathcal{M}_{\rm X}$	B (μG)
NE	relic	22%	42%	>1.7[a]	<1.43	0.8
SW	relic	14%	20%	$4.8^{+2.3}_{-0.9}$[b]	<1.57	⋯
R1	?	⋯	<4%	⋯		
R2	radio galaxy	unpol.	unpol.	⋯		
H	halo	⋯	⋯	⋯		

Notes. We include the classification, the average and maximum polarization fraction, the radio-derived and X-ray-derived Mach number, and magnetic field constraints.
[a] Constraint from polarization.
[b] Measured from spectral index.

On the basis of radio morphology, extent, and flat spectral index, R1 could be a radio galaxy; however, we did not find an optical counterpart. The flat spectral index implies that R1 is not a radio phoenix produced by adiabatic compression of fossil radio plasma by the passage of an ICM shock front or an AGN relic, originating from a fossil population caused by previous AGN activity, both of which are characterized by steep spectral indices (T. A. Enßlin & Gopal-Krishna 2001; T. A. Enßlin & M. Brüggen 2002; S. Mandal et al. 2020).

6.2. Mach Numbers for the Radio Relics

For a (quasi)-stationary-state shock (where the cooling time of electrons is much shorter than the timescale on which the shock strength changes), assuming a standard power-law energy distribution of relativistic electrons just after

Table 4
Radio Measurements for the Diffuse Radio Sources in the Cluster PSZ2 G181.06+48.47

Source	LOFAR	uGMRT		VLA	LLS[a]	α[b]	$P_{150\ \mathrm{MHz}}$	$P_{1.5\ \mathrm{GHz}}$
	$S_{144\ \mathrm{MHz}}$ (mJy)	$S_{380\ \mathrm{MHz}}$ (mJy)	$S_{700\ \mathrm{MHz}}$ (mJy)	$S_{1.5\ \mathrm{GHz}}$ (mJy)	(Mpc)		(10^{24} W Hz^{-1})	(10^{24} W Hz^{-1})
NE	29.4 ± 3.0	13.6 ± 1.0	6.8 ± 0.7	3.5 ± 0.5	∼1.3	−0.92 ± 0.04	4.81 ± 0.50	0.57 ± 0.08
SW	40 ± 4.5	14.8 ± 1.0	6.4 ± 0.6	3.3 ± 0.3	∼1.2	−1.09 ± 0.05	6.78 ± 0.77	0.56 ± 0.05
R1	9.4 ± 1.5	4.7 ± 0.4	2.6 ± 0.2	1.46 ± 0.06	∼0.25	−0.81 ± 0.05	⋯	⋯
R2	15.0 ± 2.0	3.2 ± 0.3	1.07 ± 0.05	0.33 ± 0.02	∼0.20	−1.65 ± 0.05	⋯	⋯
Halo	⋯	2.1 ± 0.3	⋯	⋯	∼1.0[c]	< -2	3	⋯

Notes. See Figures 6 and 10 for the source labeling.
[a] The LLS measured from the 144 MHz map; P is the radio power.
[b] The integrated spectral index obtained by fitting a single power law between 144 MHz and 1.5 GHz.
[c] Measured at 380 MHz.

acceleration, the integrated spectral index (α_{int}) is steeper than the injection index (α_{inj}):

$$\alpha_{\mathrm{int}} = \alpha_{\mathrm{inj}} - 0.5. \quad (6)$$

In the DSA model in the test-particle regime, the radio-integrated index is related to the Mach number ($\mathcal{M}$) of the shock as (R. Blandford & D. Eichler 1987)

$$\mathcal{M} = \sqrt{\frac{\alpha_{\mathrm{int}} - 1}{\alpha_{\mathrm{int}} + 1}}. \quad (7)$$

If generated according to the quasi-stationary shock scenario (N. S. Kardashev 1962), radio relics are expected to show a power law with spectral index $\leqslant -1$ (see Equation (6)).

The SW relic in PSZ2 G181.06+48.47 is consistent with following the stationary-state shock condition. Using Equation (7) and an integrated spectral index of -1.09 ± 0.05, we obtain a Mach number of $\mathcal{M} = 4.8^{+2.3}_{-0.9}$. For the majority of radio relics, X-ray-inferred Mach numbers are found to be below 2.5 (A. Botteon et al. 2018; A. Botteon et al. 2020; D. Wittor et al. 2021), whereas radio-derived Mach numbers are above 2.5. Recent simulations indeed suggest that shock fronts have a distribution of Mach numbers and that the Mach numbers obtained from radio-integrated spectra are biased toward the high Mach number tail of the distribution (P. Domìnguez-Fernández et al. 2019; D. Wittor et al. 2021).

The stationary-state shock condition does not hold for the NE relic because its overall spectrum is quite flat ($\alpha_{\mathrm{int}} = -0.92 \pm 0.04$). This spectrum, considering the stationary shock condition, would imply an injection spectral index of −0.42, 0.08 flatter than the flattest allowed by the DSA model. Even though Mach number predictions are not possible at these flat spectra, only a relatively strong shock will produce such a flat spectrum. Simulations consistently show that the stationary shock conditions do not hold for spherically expanding shocks (H. Kang & D. Ryu 2016) or within a turbulent medium (P. Domìnguez-Fernández et al. 2019).

An alternative method to determine the Mach number is measuring the injection index directly at the relic's leading edge from high-resolution spectral index maps. It is worth mentioning that the combination of projection effects, cooling distance, and smoothing in the radio images impacts the estimation of the injection index. Moreover, high-resolution studies of bright relics reveal that the injection index varies across the leading edge of the relic, which in turn implies that the Mach number varies across the shock front as found in simulations (D. N. Hoang et al. 2018; K. Rajpurohit et al. 2018; D. Wittor et al. 2021). We emphasize that the integrated Mach number is based on the emission-weighted spectral index distribution of the entire relic, i.e., higher Mach numbers have more weight. Mach numbers based on injection spectral index show significant variations along the relic. Therefore, the flattest injection Mach number is expected to be comparable to the integrated Mach number.

The flattest spectral index at the leading edge of the SW relic is about −0.6, which implies a shock of Mach number $\mathcal{M} \sim 4.5$ (using Equations (6) and (7)). This agrees well with the shock strength obtained from the integrated spectral index. The narrow width of the NE relic makes it difficult to measure the injection index across its leading edge.

6.3. Resolved Spectral Properties

A single spectral shape (or trajectory) in the color–color plot (Figure 8) throughout the emitting region suggests that every line of sight probes a single electron population and that conditions along each line of sight are relatively homogeneous (D. M. Katz-Stone & L. Rudnick 1997; K. Rajpurohit et al. 2021b). If data points show positive curvature, this suggests either that emitting regions are overlapping or that they have inverted spectra. Unlike some well-studied radio relics, for example, CIZA J2242.8+5301 (A. Stroe et al. 2013; G. Di Gennaro et al. 2018), RX J0603.3+4214 (R. J. van Weeren et al. 2012; K. Rajpurohit et al. 2020a), and A2744 (K. Rajpurohit et al. 2021a), we do not find a single spectral shape or trajectory in the color–color plane for the NE and SW relics.

The majority of the data points from the NE relic are clustered around the power-law line, implying negligible aging, in contrast to simple expectations of strong aging behind shock fronts. The R1 data points do not follow the same trend as the NE relic. This finding hints at the presence of distinct electron populations in these two regions, indicating that R1 and the NE relic may have different origins.

For the SW relic, we see a large scatter in the color–color plot. The color–color plots of simulated relics suggest that the locus of points changes significantly with the relic viewing angle[15] (D. Wittor et al. 2019; K. Rajpurohit et al. 2021b). In a face-on view, the relativistic electron distribution shows a wide

[15] The viewing angle is defined such that a source parallel to the plane of the sky and viewed face-on has a viewing angle of 0°, meaning that the plane of the object is parallel to the plane of the sky. A source perpendicular to the plane of the sky and viewed edge-on has a viewing angle of 90°.

scatter in the color–color plane across the relic-emitting region. However, in an edge-on view, the distribution follows a single spectral shape, indicating relatively uniform conditions along each line of sight. Therefore, the viewing angle of the SW and NE relics, on the basis of radio color–color plot trajectory (K. Rajpurohit et al. 2021b), is very likely inclined along the line of sight ($\sim$45°).

6.4. Polarization Insights

While both relics show well-aligned magnetic field vectors, the NE relic is significantly more polarized than the SW relic.

The high polarization fraction measured within the NE relic is in line with several radio relics that have been observed to exhibit a local polarization fraction of up to 65% (e.g., A. Bonafede et al. 2014; F. N. Owen et al. 2014; F. Loi et al. 2021; F. de Gasperin et al. 2022; K. Rajpurohit et al. 2020b, 2022a). The fractional polarization of radio relics is predicted to rise with increasing shock Mach numbers. According to the T. A. Ensslin et al. (1998) model, for a relic seen perfectly edge-on and assuming no further depolarization, the average fractional polarization is anticipated to increase from 40% to 60% when the Mach number increase from $\mathcal{M} = 1.5$ to $\mathcal{M} = 3$. Using a numerical model, M. Hoeft et al. (2022) and M. Kierdorf et al. (2017) found similar trends. For the NE relic, our observation shows that, at 1.5 GHz, the polarization fraction reaches values as high as 42% at 25″ resolution, which implies that the minimum Mach number in that region is 1.7 according to M. Kierdorf et al. (2017) and M. Hoeft et al. (2022).

The RM distribution across the NE relic implies very little Faraday-rotating intervening material and that the intrinsic polarization angle is well aligned with the orientation of radio emission. A possible explanation for the depolarization in the SW relic is the presence of a Faraday-rotating medium (i.e., the ICM). Interestingly, XMM-Newton images reveal faint diffuse X-ray emission at the location of R1, which is strongly depolarized between 1 and 2 GHz, suggesting that it may be situated behind or deep inside the ICM and thus is a separate feature and not physically connected to the NE relic. However, high-frequency polarization observations are required to confirm this scenario.

The average polarization fraction of radio relics is related to the viewing angle (T. A. Ensslin et al. 1998) as

$$\langle P_{\rm weak} \rangle = \frac{(s+1)}{\left(s+\frac{7}{3}\right)} \frac{\sin^2\theta}{\frac{2C^2}{C^2-1} - \sin^2\theta}, \quad (8)$$

where $\langle P_{\rm weak} \rangle$ is the mean observed polarization fraction, s is the slope of the electron energy distribution ($\alpha = \frac{1-s}{2}$), θ is the viewing angle (defined as 90° for a relic seen edge-on, i.e., perpendicular to the plane of the sky), and C is the compression factor, which is related to the spectral index by

$$C = \frac{\alpha - 2}{\alpha + \frac{1}{2}}. \quad (9)$$

Using Equation (8), we place lower limits on the viewing angle as $\theta \geqslant 42°$ and $\theta \geqslant 36°$ for the NE and SW relics, respectively. The actual values are likely to be higher owing to beam depolarization and wavelength-dependent depolarization (i.e., intrinsic and external) in the 1–2 GHz frequency range. While the polarization constraints on the viewing angle exclude extreme scenarios in which the relics are viewed face-on, the merger might not be happening in the plane of the sky, but rather at an inclination $\sim$45° with respect to the plane of the sky.

6.5. A Candidate Halo

We investigate the potential presence of a radio halo in PSZ2 G181.06+48.47. As shown in the right panel of Figure 10, we find a low-significance detection of diffuse emission toward the cluster center in the low-resolution uGMRT 380 MHz image. It has an LLS of about 1.1 Mpc (2σ). The total flux density of the central diffuse emission is $S_{380\,\rm MHz} = 2.1 \pm 0.3$ mJy (2σ) and $S_{700\,\rm MHz} < 0.6$ mJy (2σ upper limit). We can therefore set an upper limit on the spectral index of $\alpha^{700\,\rm MHz}_{380\,\rm MHz} \leqslant -2.0$. By extrapolating from the radio spectrum, we expect a flux density of about 15 mJy at 144 MHz, corresponding to a radio power of $P_{144\,\rm MHz} \leqslant 3 \times 10^{24}$ W Hz^{-1}. However, the halo emission is not detected in the LOFAR data. The missing flux density at 144 MHz is very likely related to calibration issue, as this region shows negative flux density when imaged at low resolution. Another possible explanation is that the spectrum of the halo may be curved, i.e., it is flatter below 400 MHz, as is seen for the radio halo in the Coma cluster (M. Thierbach et al. 2003), AS1063 (C. Xie et al. 2020), and MACS J0717.5+3745 (K. Rajpurohit et al. 2022a).

Only a handful of radio halos have been found in low-mass clusters ($M_{500} \leqslant 5 \times 10^{14}\ M_\odot$), for example, A1430 (M. Hoeft et al. 2021), PSZ2 G145.92–12.53 (A. Botteon et al. 2021), A1451 (V. Cuciti et al. 2018), A990 (D. N. Hoang et al. 2021), and Zwcl 0634.1+4750 (V. Cuciti et al. 2018). Detecting such halos is challenging owing to the low energy budgets available to inject large-scale cluster turbulence into the ICM. The radio power of the candidate halo in PSZ2 G181.06+48.47 is in line with the 144 MHz radio power versus mass relation of known halos (R. J. van Weeren et al. 2021; V. Cuciti et al. 2023; S. W. Duchesne et al. 2024).

According to the turbulent reacceleration models, radio halos with ultrasteep spectra are produced by less energetic mergers and in low-mass systems as the cluster mass impacts the energy budget for particle acceleration (R. Cassano & G. Brunetti 2005; G. Brunetti & T. W. Jones 2014). Therefore, the presence of an ultra–steep-spectrum radio halo in a low-mass cluster PSZ2 G181.06+48.47 is in line with turbulent reacceleration models. J. Donnert et al. (2013) investigated the evolution of radio halos during cluster mergers and found that radio halos are brighter and have flat spectral indices ($\alpha \geqslant -1.3$) in early merger stages, transitioning to fainter halos with steeper spectral indices ($\alpha \leqslant -1.5$) in later merger stages (after a few Gyr). The properties of the candidate radio halo PSZ2 G181.06+48.47 are consistent with it being in an inefficient acceleration stage.

6.6. Acceleration Efficiency

We investigate the acceleration efficiencies required to reproduce the observed relic luminosities in a DSA scenario with acceleration by a stationary shock from the thermal pool. We follow the formalism described in M. Hoeft & M. Brüggen (2007) to predict the radio relic power from the properties of the downstream plasma. The fraction of the kinetic energy channeled into accelerated thermal pool electrons ξ_e

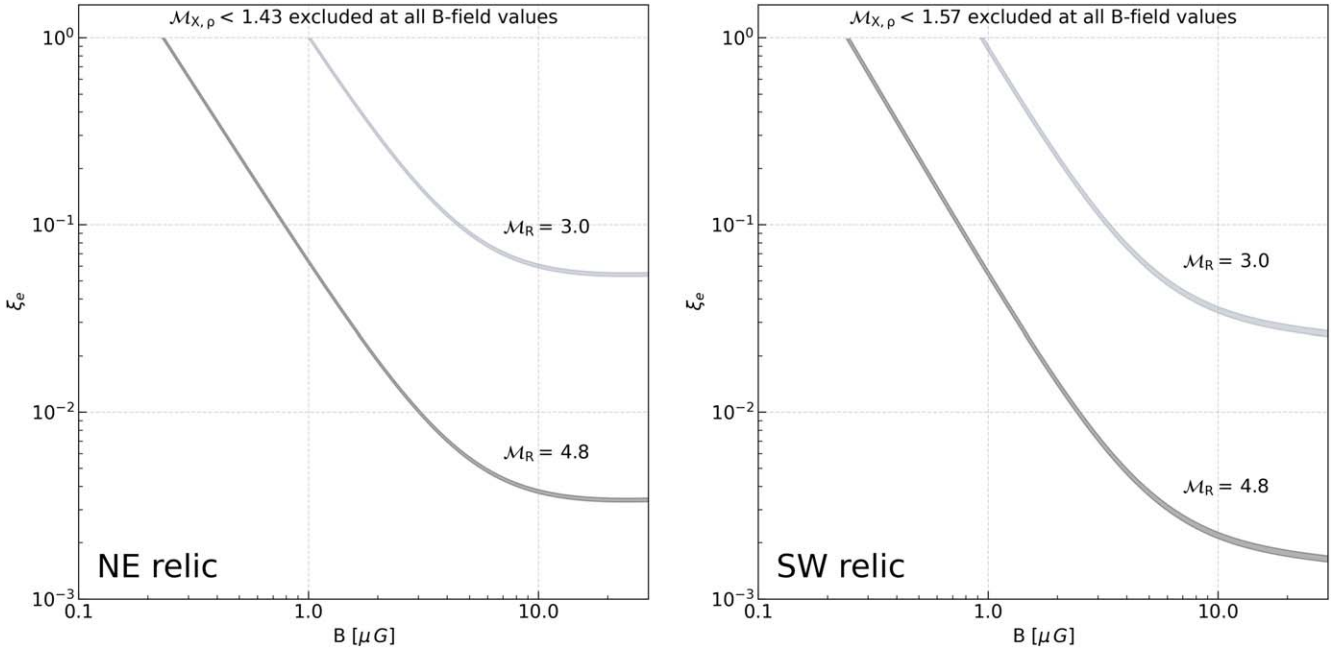

Figure 11. Electron acceleration efficiency as a function of magnetic field in the downstream region. Radio and X-ray Mach numbers are considered. DSA from the thermal pool is compatible with favorable scenarios ($B \gtrsim 1$ μG and $\mathcal{M} \gtrsim 4.8$), but reacceleration needs to otherwise be invoked to explain the bright and distant relics.

(acceleration efficiency) is computed as

$$\xi_e = \frac{1}{C} \cdot \left(\frac{P}{\mathrm{W\,Hz^{-1}}}\right) \cdot \left(\frac{A}{\mathrm{Mpc^3}}\right)^{-1} \cdot \left(\frac{n_{e,d}}{10^{-4}\mathrm{cm^{-3}}}\right)^{-1} \cdot \left(\frac{T_d}{7\,\mathrm{keV}}\right)^{-\frac{3}{2}} \cdot \left(\frac{\nu}{1.4\,\mathrm{GHz}}\right)^{-\alpha} \cdot \left(\frac{B}{\mu\mathrm{G}}\right)^{1+\alpha} \cdot \left(\frac{B_{\mathrm{CMB}}^2}{B^2} + 1\right) \cdot \Psi(\mathcal{M}, T_d), \quad (10)$$

where C is a constant equal to 1.28×10^{27} (K. Rajpurohit et al. 2021a), P is the radio power calculated from Equation (4), A is the relic area calculated as $\pi/4 \cdot \mathrm{LLS}^2$ (M. Hoeft & M. Brüggen 2007; K. Rajpurohit et al. 2021a), $n_{e,d}$ and T_d are the downstream electron density and temperature, respectively, ν is the observing frequency, α is the integrated radio spectrum, B is the magnetic field, and B_{CMB} is the B-field strength equivalent to the cosmic microwave background energy density at the redshift of the cluster ($B_{\mathrm{CMB}} = 3.24 \cdot (1+z)^2$ μG). $\Psi(\mathcal{M}, T_d)$ describes the strong dependency on the Mach number $\mathcal{M}$ and a mild dependency on the downstream temperature T_d.

We explored the dependency of the acceleration efficiency ξ_e on the magnetic field for a range of B-field values. The radio power P at $\nu = 1.5$ GHz, relic area A, and integrated spectral index α are calculated directly from the radio data. We assume $n_{e,d} = 10^{-4}\,\mathrm{cm^{-3}}$. We use the X-ray measurement of the downstream temperatures from A. Stroe et al. (2025). Based on these T_d values, $\Psi(\mathcal{M}, T_d)$ was then derived from M. Hoeft & M. Brüggen (2007) for a range of Mach numbers, including the radio-derived Mach number for the SW relic ($\mathcal{M}_R = 4.8$), a typical Mach number for relics ($\mathcal{M}_R = 3$), and the 5σ X-ray Mach number upper limits derived from the density jumps in the XMM-Newton data ($\mathcal{M}_{\mathrm{X},\rho} = 1.43$ and $\mathcal{M}_{\mathrm{X},\rho} = 1.57$ for the NE and SW relics, respectively; A. Stroe et al. 2025). We show the electron acceleration efficiency required to reproduce the observed radio power of the two relics in Figure 11.

Simulations predict that CR acceleration efficiencies from the thermal pool depend strongly on Mach number, with $\lesssim 10^{-4}$ for $\mathcal{M} < 3$ and reaching 10^{-4} to 10^{-3} for $\mathcal{M} > 3$ (H. Kang et al. 2007; H. Kang & D. Ryu 2013). Under the assumption that CRe are injected from the same thermal population as the cosmic rays proton, realistic ξ_e values are expected to be $<10^{-2}$, with optimistic values still under 0.1 (e.g., A. Botteon et al. 2020, and references therein). Unrealistically large CRe efficiencies are thus required to reproduce the large observed luminosities of known radio relics given their association with weak shocks ($\mathcal{M} < 5$, with most cases $\mathcal{M} < 3$; e.g., A. Botteon et al. 2020).

For PSZ2 G181.06+48.47, the scenarios based on the density-derived Mach number are excluded under all B-field assumptions, as required efficiencies are above 100%. With compression and amplification, magnetic fields in radio relics are expected to be at the few μG levels (1–6 μG; e.g., A. Finoguenov et al. 2010; R. J. van Weeren et al. 2010; K. Rajpurohit et al. 2018; C. Stuardi et al. 2021). Given the $\sim$0.6 μG B-field derived from the polarization and assuming amplification factors of a few (e.g., L. Iapichino & M. Brüggen 2012; J. M. F. Donnert et al. 2016a), the magnetic field in the relics is expected to not exceed a few μG. Under the optimistic assumption that the B-field is at the few μG level, neither of the two relics can be reproduced with realistic efficiencies of $\xi_e \sim 10^{-2}$. If the magnetic field or Mach number is smaller (e.g., $B < 1$ μG and $\mathcal{M} < 4.8$), the required efficiency is higher ($\xi_e \gtrsim 1$). Further, simulations suggest that Mach numbers measured from the radio observations (as per Equation (7)) trace the tail of the high Mach number distribution in relics and that only a small fraction of the relic area is expected to have such high Mach numbers (e.g., A. Botteon et al. 2020; D. Wittor et al. 2021), resulting in even more stringent efficiency requirements for the NE and SW relics in PSZ2 G181.06+48.47 (e.g., lowering the covering fraction

from 100% to 50% doubles the ξ_e requirement). A patchy surface brightness distribution, like the one we might be observing in NE, could be a sign of an especially high coverage fraction with small Mach numbers (P. Domìnguez-Fernández et al. 2024). Therefore, even under the most optimistic assumptions, the relic luminosities can only be reproduced if $\xi_e \sim 0.1$ efficiencies are invoked.

Despite being located above the luminosity–cluster mass relation (A. Stroe et al. 2025), the NE and SW relics are at least ∼5–50 times less luminous than bright relics, such as those in CIZA J2242.8+5301 (A. Stroe et al. 2013; G. Di Gennaro et al. 2018), RX J0603.3+4214 (R. J. van Weeren et al. 2012; K. Rajpurohit et al. 2020a), A2256 (K. Rajpurohit et al. 2022b), or A3667 (F. de Gasperin et al. 2022). However, the combination of the large clustercentric distances and the low cluster mass results in low (1–2 keV) downstream temperatures, which means that the required efficiencies for NE and SW are still high if particles are accelerated from the thermal pool and if the Mach number of the shock is below 4. In that case, both relics in PSZ2 G181.06+48.47 are difficult to explain in a simple DSA scenario from the thermal pool. The low acceleration efficiency can be mitigated if some sort of preacceleration of CRe is taken into account, which can result in a significant boost of the radio luminosity. That can include, for example, shock reacceleration of a preexisting fossil population of seed electrons from AGN activity or reacceleration by multiple shocks (e.g., A. Stroe et al. 2014; R. J. van Weeren et al. 2017; H. Kang 2021; G. Inchingolo et al. 2022; D. C. Smolinski et al. 2023).

6.7. Origin of the Diffuse Emission

The alignment between the elongated X-ray emission (A. Stroe et al. 2025), the WL mass distribution (E. Ahn et al. 2025), and the two prominent relics to the north and south of the cluster implies a post-core binary merger in the general N–NE to S–SW direction. The large 2.6 Mpc projected distance between the NE and SW relics prefers a late-stage merger, maybe seen post-apocenter, as the subclusters are moving back toward each other (M. Hoeft et al. 2004; R. J. van Weeren et al. 2011a; K. Y. Ng et al. 2015; W. Lee et al. 2024). However, a more detailed analysis of all the observations available reveals that a more complicated merger scenario is at play in PSZ2 G181.06+48.47. The elongated shape with a high aspect ratio between the long and short sides of the relics would naively suggest that they are seen close to edge-on, suggesting that the merger is happening in the plane of the sky. However, insights from the polarization and radio color–color plot suggest that the relics are viewed at an inclination ∼45° with respect to the plane of the sky. Such a high viewing angle results in a much larger physical separation between the relic of up to ∼3.5 Mpc. To our knowledge, this is the largest relic separation ever found. The possible merger scenarios, including an outgoing merger after the second collision and a returning merger after the first apocenter, are discussed in E. Ahn et al. (2025).

In some simple, binary, head-on collisions, a clear alignment between the orientations of the radio galaxies and the merger axis can be observed (e.g., CIZA J2242.8+5301; R. J. van Weeren et al. 2011a; A. Stroe et al. 2013; M. J. Jee et al. 2015). During the merger, as galaxies decouple from the ICM, tails of radio galaxies trace their relative motion with respect to the tenuous hot gas. We observe no such clear alignment in PSZ2 G181.06+48.47. The tails of the two cleanly resolved radio-emitting cluster members, R2 and the prominent wide-angle tailed source almost directly north, are roughly aligned on the N–S direction at an angle of ∼15° and ∼40°, respectively, from the merger axis inferred from the ICM, WL, and radio relics (A. Stroe et al. 2025; E. Ahn et al. 2025). However, the morphology and spectral index trends across these two sources indicate that they are both moving roughly northward relative to the ICM in their vicinity. The tailed radio sources seem to be consistent with a late-stage, returning merger scenario, in which the subclusters are falling back toward each other after reaching the maximum separation after the first core passage.

The NE relic has some features typically associated with relics, including its broad arc-like morphology and high polarization fraction. However, the relic's flat spectral index is inconsistent with the standard DSA from the thermal pool. Moreover, the radio polarization and X-ray analysis suggest a relatively weak shock ($\mathcal{M} \sim 1.8$) associated with the NE relic, requiring unrealistic acceleration efficiency if the CRe are accelerated from the thermal pool. A flat spectral index and lack of a clear spectral index gradient behind the shock front across NE indicate a young population of electrons. While the ∼45° viewing angle is difficult to reconcile with the narrow relic width, it can help explain the lack of a clear spectral index trend. The evidence supports the reacceleration scenario.

However, none of the AGN embedded in the NE relic appear to be morphologically connected to it, so it is unclear what could be the source of seed electrons. We note that the reacceleration of "ghost" plasma (i.e., fossil plasma from an AGN that is not detected with current telescopes owing to low energy) is still possible. If the NE relic is formed owing to the MSS, a break in the overall spectral is expected at 1.4 GHz (G. Inchingolo et al. 2022). Future high-frequency observations would be critical to ascertain the viability of the MSS for the NE relic.

In contrast to the NE relic, the SW relic shows a clear spectral index gradient toward the cluster center and a high polarization fraction, as expected in the DSA model. However, there is a large discrepancy in the radio- and X-ray-estimated Mach numbers that is reported for several other relics. This mismatch can be explained by the fact that the radio and X-ray observations trace different parts of the Mach number distribution as revealed by simulations.

A reacceleration scenario is also possible for the SW relic. The radio emission from the SW relic extends to the east of radio galaxy R2. At the location of the relic, the spectral index again flattens, which may suggest that R2 is providing seed electrons to the relic. A similar change in the spectral index distribution is observed for the relics and nearby radio galaxies in PLCK G287.0+32.9 (A. Bonafede et al. 2014), RXC J1314.4–2515 (C. Stuardi et al. 2019), and CIZA J2242.8+5301 (G. Di Gennaro et al. 2018). However, it is not obvious that the injection of fossil electrons by one radio galaxy can produce a uniform population of electrons forming a ∼1.3 Mpc large relic. Moreover, the flatter spectral index observed at the southern tip of the R2 tail could be simply due to projection effects. With the current data, we cannot rule out that the connection between the SW relic and the tailed radio galaxy is simply due to projection. However, if reacceleration is invoked, that would alleviate the tight constraints on the acceleration efficiency necessary to reproduce the relic brightness.

Moreover, the reacceleration would also explain the large discrepancy between the X-ray- and radio-derived Mach number for the SW relic, since the former traces the most recent shock, while the latter reflects the cumulative effect of all events (H. Kang 2021). Such a scenario would require the main merger-induced shock produced after the core passage to be followed by other shocks, such as an accretion shock, supporting, for example, a more complex merging scenario involving another infalling subcluster.

Further, compared to more common arc-like morphologies (A. Bonafede et al. 2009; F. de Gasperin et al. 2014; D. N. Hoang et al. 2018; K. Rajpurohit et al. 2024), where relics are thought to trace outward-traveling shock waves induced in (nearly) head-on mergers, the SW relic features an inverted morphology, bowing away from the cluster, which suggests a more complex merger history. Similar types of inverted morphology are observed in a handful of relics, e.g., in A3266 (C. J. Riseley et al. 2022), Coma (A. Bonafede et al. 2022), and PSZ2 G145.92–12.53 (A. Botteon et al. 2021). Recent simulations propose that the "inverted morphology" can form when an outward-traveling shock wave is bent inward by an infalling galaxy cluster or group (L. M. Böss et al. 2023; W. Lee et al. 2024), lending further support to a more complex merger.

The lack of an optical counterpart and the relatively flat spectrum rule out a radio phoenix or AGN relic scenarios for R1, so its nature remains a mystery. A low surface brightness bridge linking the NE relic to R1 indicates a physical connection. One possible explanation is that R1 is associated with the NE relic, as relics are known to show diverse morphologies. However, a strong depolarization across R1 and very different RMs (although only a small patch is detected) suggests that R1 and NE are separated in Faraday space, i.e., not physically connected. The different trends in the color–color plot across these two structures further support this. R1 may be a radio galaxy. However, we do not find any obvious optical host. There is also a background cluster (RM J093941.1 +405205.9) to the northwest of R1 located at a redshift of $z = 0.50$ (A. Stroe et al. 2025). If R1 is associated with the background cluster, its LLS would be ∼600 kpc. Therefore, R1 could be a relic associated with the background cluster, located about 1 Mpc from the cluster center. In conclusion, the nature of R1 is uncertain.

Finally, the presence of a possible faint, steep-spectrum radio halo coincident with the X-ray ICM serves as further evidence that PSZ2 G181.06+48.47 is an evolved merger.

7. Conclusions

In this paper we have presented deep, multifrequency, wide-band uGMRT and VLA radio observations of the low-mass, merging galaxy cluster PSZ2 G181.06+48.47. We combined these observations with the published LOFAR data to study the origin of the diffuse emission in the cluster. The cluster was previously classified as a merging system by means of X-ray and optical studies (A. Botteon et al. 2022). The two giant diffuse radio sources are located along the merger axis, separated by about 3.5 Mpc—the largest known to date.

Based on our new images, we classify the previously known diffuse radio sources (NE and SW) as radio relics. The NE relic is consistent with an arc-shaped morphology, follows a power-law spectrum, and is strongly polarized at 1–2 GHz, indicating a weak shock of $\mathcal{M} \sim 1.7$. The magnetic field vectors are aligned with the orientation of the radio emission, as expected owing to compression by the passage of the merger shock wave. However, the unusually flat spectral index ($\alpha = -0.92 \pm 0.04$) behavior up to high frequencies and the unrealistic acceleration efficiency requirements are in tension with the DSA model in the test-particle regime. The NE relic can be explained by reacceleration scenarios.

The SW relic shows an "inverted morphology" and exhibits a clear spectral index gradient toward the cluster center. Patches of polarized emission are detected across the SW relic, and its integrated radio spectrum is consistent with particle acceleration at the shock of $\mathcal{M} \sim 4.8$ by the DSA in the test-particle regime.

The $\theta \sim 45°$ viewing angle derived from the polarization and the radio color–color plot for the NE and SW relic imply that the merger might not be happening in the plane of the sky. Our results suggest that the cluster is in an evolved merger state, likely seen post-apocenter. However, given the current limitations in multiwavelength data, it is difficult to determine which merger scenario is more likely. If this is the case, the system requires different merging scenarios compared to the edge-on-viewed relics.

Low-resolution uGMRT Band 3 images reveal significant (2σ) diffuse emission around the cluster center region (about 1 Mpc). From the nondetection at uGMRT Band 4, we set an upper limit on the spectral index at $\alpha \leqslant -2$. The radio power of this emission lies on the known power versus mass relations for radio halos. We classify this emission as a candidate radio halo.

To the north of the NE relic, we find a 370 kpc (assuming the cluster redshift) diffuse radio source (R1) connecting to the NE relic via a faint bridge-like emission. Its exact nature is unknown. R1 could be a radio galaxy or a radio relic associated with a background cluster.

Only a limited number of clusters with mass $\leqslant 5 \times 10^{14}\ M_{\odot}$ are known to host diffuse radio sources. This lower mass range remains largely unexplored owing to observational limitations. However, their numbers are increasing thanks to a new generation of telescopes. The discovery of fainter double relics in the low-mass cluster PSZ2 G181.06+48.47 with the largest relic separation suggests that we are entering into a new territory and that the Square Kilometre Array will be a game changer for detecting and understanding the origins of diffuse radio sources in low-mass clusters.

Acknowledgments

We thank Hiroki Akamatsu and Grant Tremblay for useful discussions. A.S. gratefully acknowledges the support of a Clay Fellowship and the NASA 80NSSC21K0822 and Chandra GO0-21122X grants. M.J.J. acknowledges support for the current research from the National Research Foundation (NRF) of Korea under the programs 2022R1A2C1003130 and RS-2023-00219959. L.L. acknowledges the financial contribution from the INAF grant 1.05.12.04.01. This work is based on observations from GMRT, which is run by the National Centre for Radio Astrophysics (NCRA) of the Tata Institute of Fundamental Research (TIFR). This research has made use of observations from the VLA, which is operated by the National Radio Astronomy Observatory, a facility of the National Science Foundation operated under cooperative agreement by Associated Universities. This work used LOFAR observations, which was designed and constructed by ASTRON. This work has also made use of observations with the Chandra X-ray

Observatory and XMM-Newton, an ESA science mission with instruments and contributions directly funded by ESA Member States and the US (NASA).

Facilities: VLA, GMRT, LOFAR, XMM, CXO, SDSS.

Software: Astropy (Astropy Collaboration et al. 2013, 2018), APLpy (T. Robitaille & E. Bressert 2012), Matplotlib (J. D. Hunter 2007), TOPCAT (M. B. Taylor 2005), DS9 (W. A. Joye & E. Mandel 2003), CASA (CASA Team et al. 2022).

ORCID iDs

Kamlesh Rajpurohit https://orcid.org/0000-0001-7509-2972
Andra Stroe https://orcid.org/0000-0001-8322-4162
Ewan O'Sullivan https://orcid.org/0000-0002-5671-6900
Eunmo Ahn https://orcid.org/0009-0009-4676-7868
Wonki Lee https://orcid.org/0000-0002-1566-5094
Hyejeon Cho https://orcid.org/0000-0001-5966-5072
M. James Jee https://orcid.org/0000-0002-5751-3697
Reinout van Weeren https://orcid.org/0000-0002-0587-1660
Lorenzo Lovisari https://orcid.org/0000-0002-3754-2415
Kyle Finner https://orcid.org/0000-0002-4462-0709
Aurora Simionescu https://orcid.org/0000-0002-9714-3862
William Forman https://orcid.org/0000-0002-9478-1682
Timothy Shimwell https://orcid.org/0000-0001-5648-9069
Christine Jones https://orcid.org/0000-0003-2206-4243
Zhenlin Zhu https://orcid.org/0000-0001-8812-8284
Scott Randall https://orcid.org/0000-0002-3984-4337

References

Ahn, E., Cho, H., Jee, M. J., et al. 2025, ApJ, 984, 26
Albuquerque, R. P., Machado, R. E. G., & Monteiro-Oliveira, R. 2024, MNRAS, 530, 2146
Almeida, A., Anderson, S. F., Argudo-Fernández, M., et al. 2023, ApJS, 267, 44
Astropy Collaboration, Price-Whelan, A. M., Sipőcz, B. M., et al. 2018, AJ, 156, 123
Astropy Collaboration, Robitaille, T. P., Tollerud, E. J., et al. 2013, A&A, 558, A33
Blandford, R., & Eichler, D. 1987, PhR, 154, 1
Bonafede, A., Brüggen, M., van Weeren, R., et al. 2012, MNRAS, 426, 40
Bonafede, A., Brunetti, G., Rudnick, L., et al. 2022, ApJ, 933, 218
Bonafede, A., Cassano, R., Brüggen, M., et al. 2017, MNRAS, 470, 3465
Bonafede, A., Giovannini, G., Feretti, L., Govoni, F., & Murgia, M. 2009, A&A, 494, 429
Bonafede, A., Intema, H. T., Brüggen, M., et al. 2014, ApJ, 785, 1
Bonafede, A., Vazza, F., Brüggen, M., et al. 2013, MNRAS, 433, 3208
Böss, L. M., Steinwandel, U. P., & Dolag, K. 2023, ApJL, 957, L16
Botteon, A., Brunetti, G., van Weeren, R. J., et al. 2020, ApJ, 897, 93
Botteon, A., Cassano, R., van Weeren, R. J., et al. 2021, ApJL, 914, L29
Botteon, A., Gastaldello, F., & Brunetti, G. 2018, MNRAS, 476, 5591
Botteon, A., Gastaldello, F., Brunetti, G., & Kale, R. 2016, MNRAS, 463, 1534
Botteon, A., Shimwell, T. W., Cassano, R., et al. 2022, A&A, 660, A78
Brentjens, M. A., & de Bruyn, A. G. 2005, A&A, 441, 1217
Brunetti, G., & Jones, T. W. 2014, IJMPD, 23, 1430007
Brunetti, G., & Lazarian, A. 2007, MNRAS, 378, 245
Brunetti, G., Setti, G., Feretti, L., & Giovannini, G. 2001, MNRAS, 320, 365
Bruno, L., Rajpurohit, K., Brunetti, G., et al. 2021, A&A, 650, A44
CASA Team, Bean, B., Bhatnagar, S., et al. 2022, PASP, 134, 114501
Cassano, R., & Brunetti, G. 2005, MNRAS, 357, 1313
Chandra, P., Ray, A., & Bhatnagar, S. 2004, ApJ, 612, 974
Chatterjee, S., Rahaman, M., Datta, A., Kale, R., & Paul, S. 2024, MNRAS, 527, 10986
Cho, H., James Jee, M., Smith, R., Finner, K., & Lee, W. 2022, ApJ, 925, 68
Cornwell, T. J., Golap, K., & Bhatnagar, S. 2008, ISTSP, 2, 647
Cuciti, V., Brunetti, G., van Weeren, R., et al. 2018, A&A, 609, A61
Cuciti, V., Cassano, R., Sereno, M., et al. 2023, A&A, 680, A30
Dabhade, P., Röttgering, H. J. A., Bagchi, J., et al. 2020, A&A, 635, A5
Dawson, W. A. 2013, ApJ, 772, 131
de Gasperin, F., Intema, H. T., van Weeren, R. J., et al. 2015, MNRAS, 453, 3483
de Gasperin, F., Rudnick, L., Finoguenov, A., et al. 2022, A&A, 659, A146
de Gasperin, F., van Weeren, R. J., Brüggen, M., et al. 2014, MNRAS, 444, 3130
Di Gennaro, G., van Weeren, R. J., Hoeft, M., et al. 2018, ApJ, 865, 24
Di Gennaro, G., van Weeren, R. J., Rudnick, L., et al. 2021, ApJ, 911, 3
Domìnguez-Fernández, P., Brüggen, M., Vazza, F., et al. 2021, MNRAS, 507, 2714
Domìnguez-Fernández, P., Ryu, D., & Kang, H. 2024, A&A, 685, A68
Domìnguez-Fernández, P., Vazza, F., Brüggen, M., & Brunetti, G. 2019, MNRAS, 486, 623
Donnert, J., Dolag, K., Brunetti, G., & Cassano, R. 2013, MNRAS, 429, 3564
Donnert, J. M. F., Stroe, A., Brunetti, G., Hoang, D., & Roettgering, H. 2016a, MNRAS, 462, 2014
Donnert, J., Vazza, F.., Brüggen, M., & ZuHone, J. 2016b, SSRv, 8, 122
Drury, L. O. 1983, RPPh, 46, 973
Duchesne, S. W., Botteon, A., Koribalski, B. S., et al. 2024, PASA, 41, e026
Ensslin, T. A., Biermann, P. L., Klein, U., & Kohle, S. 1998, A&A, 332, 395
Enßlin, T. A., & Brüggen, M. 2002, MNRAS, 331, 1011
Enßlin, T. A., & Gopal-Krishna 2001, in ASP Conf. Ser. 250, Particles and Fields in Radio Galaxies Conf., ed. R. A. Laing & K. M. Blundell (San Francisco, CA: ASP), 454
Finoguenov, A., Sarazin, C. L., Nakazawa, K., Wik, D. R., & Clarke, T. E. 2010, ApJ, 715, 1143
Flewelling, H. A., Magnier, E. A., Chambers, K. C., et al. 2020, ApJS, 251, 7
Giovannini, G., & Feretti, L. 2004, JKAS, 37, 323
Golovich, N., Dawson, W. A., Wittman, D. M., et al. 2019, ApJ, 882, 69
Gupta, Y., Ajithkumar, B., Kale, H. S., et al. 2017, CSci, 113, 707
Ha, J.-H., Ryu, D., & Kang, H. 2018, ApJ, 857, 26
Hoang, D. N., Shimwell, T. W., Osinga, E., et al. 2021, MNRAS, 501, 576
Hoang, D. N., Shimwell, T. W., Stroe, A., et al. 2017, MNRAS, 471, 1107
Hoang, D. N., Shimwell, T. W., van Weeren, R. J., et al. 2018, MNRAS, 478, 2218
Hoeft, M., & Brüggen, M. 2007, MNRAS, 375, 77
Hoeft, M., Brüggen, M., & Yepes, G. 2004, MNRAS, 347, 389
Hoeft, M., Dumba, C., Drabent, A., et al. 2021, A&A, 654, A68
Hoeft, M., Rajpurohit, K., Wittor, D., di Gennaro, G., & Domìnguez-Fernández, P. 2022, Galax, 10, 10
Hunter, J. D. 2007, CSE, 9, 90
Hutschenreuter, S., Anderson, C. S., Betti, S., et al. 2022, A&A, 657, A43
Iapichino, L., & Brüggen, M. 2012, MNRAS, 423, 2781
Inchingolo, G., Wittor, D., Rajpurohit, K., & Vazza, F. 2022, MNRAS, 509, 1160
Intema, H. T., van der Tol, S., Cotton, W. D., et al. 2009, A&A, 501, 1185
Jee, M. J., Dawson, W. A., Stroe, A., et al. 2016, ApJ, 817, 179
Jee, M. J., Stroe, A., Dawson, W., et al. 2015, ApJ, 802, 46
Jones, A., de Gasperin, F., Cuciti, V., et al. 2023, A&A, 680, A31
Jonas, J. & MeerKAT Team 2016, in Proc. of MeerKAT Science: On the Pathway to the SKA (Trieste: SISSA), 1
Joye, W. A., & Mandel, E. 2003, in ASP Conf. Ser. 295, Astronomical Data Analysis Software and Systems XII, ed. H. E. Payne, R. I. Jedrzejewski, & R. N. Hook (San Francisco, CA: ASP), 489
Kang, H. 2016, JKAS, 49, 83
Kang, H. 2021, JKAS, 54, 103
Kang, H., & Ryu, D. 2011, ApJ, 734, 18
Kang, H., & Ryu, D. 2013, ApJ, 764, 95
Kang, H., & Ryu, D. 2016, ApJ, 823, 13
Kang, H., Ryu, D., Cen, R., & Ostriker, J. P. 2007, ApJ, 669, 729
Kardashev, N. S. 1962, SvA, 6, 317
Katz-Stone, D. M., & Rudnick, L. 1997, ApJ, 488, 146
Katz-Stone, D. M., Rudnick, L., & Anderson, M. C. 1993, ApJ, 407, 549
Kierdorf, M., Beck, R., Hoeft, M., et al. 2017, A&A, 600, A18
Kim, J., Jee, M. J., Hughes, J. P., et al. 2021, ApJ, 923, 101
Knowles, K., Cotton, W. D., Rudnick, L., et al. 2022, A&A, 657, A56
Knowles, K., Intema, H. T., Baker, A. J., et al. 2016, MNRAS, 459, 4240
Koester, B. P., McKay, T. A., Annis, J., et al. 2007, ApJ, 660, 239
Lee, W., James Jee, M., Finner, K., et al. 2022, ApJ, 924, 18
Lee, W., Jee, M. J., Kang, H., et al. 2020, ApJ, 894, 60
Lee, W., Pillepich, A., ZuHone, J., et al. 2024, A&A, 686, A55
Loi, F., Murgia, M., Vacca, V., et al. 2021, MNRAS, 501, 3183
Mandal, S., Intema, H. T., van Weeren, R. J., et al. 2020, A&A, 634, A4
Markevitch, M., & Vikhlinin, A. 1997, ApJ, 491, 467

McMullin, J. P., Waters, B., Schiebel, D., Young, W., & Golap, K. 2007, in ASP Conf. Ser. 376, Astronomical Data Analysis Software and Systems XVI, ed. R. A. Shaw, F. Hill, & D. J. Bell (San Francisco, CA: ASP), 127
Mohan, N., & Rafferty, D. 2015, PyBDSM: Python Blob Detection and Source Finder, Astrophysics Source Code Library, ascl:1502.007
Murgia, M., Govoni, F., Feretti, L., et al. 2004, A&A, 424, 429
Murgia, M., Govoni, F., Vacca, V., et al. 2024, MNRAS, 528, 6470
Ng, K. Y., Dawson, W. A., Wittman, D., et al. 2015, MNRAS, 453, 1531
Nuza, S. E., Gelszinnis, J., Hoeft, M., & Yepes, G. 2017, MNRAS, 470, 240
Ochsenbein, F., Bauer, P., & Marcout, J. 2000, A&AS, 143, 23
Offringa, A. R., de Bruyn, A. G., Biehl, M., et al. 2010, MNRAS, 405, 155
Offringa, A. R., McKinley, B., Hurley-Walker, N., et al. 2014, MNRAS, 444, 606
Offringa, A. R., & Smirnov, O. 2017, MNRAS, 471, 301
Owen, F. N., Rudnick, L., Eilek, J., et al. 2014, ApJ, 794, 24
Parekh, V., Thorat, K., Kale, R., et al. 2020, MNRAS, 499, 404
Paul, S., Gupta, P., Salunkhe, S., et al. 2021, MNRAS, 506, 5389
Paul, S., John, R. S., Gupta, P., & Kumar, H. 2017, MNRAS, 471, 2
Paul, S., Kale, R., Datta, A., et al. 2023, JApA, 44, 38
Perley, R. A., & Butler, B. J. 2013, ApJS, 204, 19
Petrosian, V. 2001, ApJ, 557, 560
Planck Collaboration, Ade, P. A. R., Aghanim, N., et al. 2016, A&A, 594, A13
Rajpurohit, K., Hoeft, M., van Weeren, R. J., et al. 2018, ApJ, 852, 65
Rajpurohit, K., Hoeft, M., Vazza, F., et al. 2020a, A&A, 636, A30
Rajpurohit, K., Hoeft, M., Wittor, D., et al. 2022a, A&A, 657, A2
Rajpurohit, K., Lovisari, L., Botteon, A., et al. 2024, ApJ, 966, 38
Rajpurohit, K., van Weeren, R. J., Hoeft, M., et al. 2022b, ApJ, 927, 80
Rajpurohit, K., Vazza, F., Hoeft, M., et al. 2020b, A&A, 642, L13
Rajpurohit, K., Vazza, F., van Weeren, R. J., et al. 2021a, A&A, 654, A41
Rajpurohit, K., Wittor, D., van Weeren, R. J., et al. 2021b, A&A, 646, A56
Rau, U., & Cornwell, T. J. 2011, A&A, 532, A71
Riseley, C. J., Bonnassieux, E., Vernstrom, T., et al. 2022, MNRAS, 515, 1871
Robitaille, T., & Bressert, E. 2012, APLpy: Astronomical Plotting Library in Python, Astrophysics Source Code Library, ascl:1208.017
Roettiger, K., Burns, J. O., & Stone, J. M. 1999, ApJ, 518, 603
Rykoff, E. S., Rozo, E., Busha, M. T., et al. 2014, ApJ, 785, 104
Sarazin, C. L., Finoguenov, A., & Wik, D. R. 2013, AN, 334, 346
Scaife, A. M. M., & Heald, G. H. 2012, MNRAS, 423, L30
Shimwell, T. W., Hardcastle, M. J., Tasse, C., et al. 2022, A&A, 659, A1
Shimwell, T. W., Markevitch, M., Brown, S., et al. 2015, MNRAS, 449, 1486
Shimwell, T. W., Tasse, C., Hardcastle, M. J., et al. 2019, A&A, 622, A1
Sikhosana, S. P., Hilton, M., Bernardi, G., et al. 2024, arXiv:2404.03944
Sikhosana, S. P., Knowles, K., Hilton, M., Moodley, K., & Murgia, M. 2023, MNRAS, 518, 4595
Skillman, S. W., Hallman, E. J., O'Shea, B. W., et al. 2011, ApJ, 735, 96
Skillman, S. W., Xu, H., Hallman, E. J., et al. 2013, ApJ, 765, 21
Smolinski, D. C., Wittor, D., Vazza, F., & Brüggen, M. 2023, MNRAS, 526, 4234
Sokoloff, D. D., Bykov, A. A., Shukurov, A., et al. 1998, MNRAS, 299, 189
Stroe, A., Harwood, J. J., Hardcastle, M. J., & Röttgering, H. J. A. 2014, MNRAS, 445, 1213
Stroe, A., Rajpurohit, K., Zhu, Z., et al. 2025, ApJ, 984, 24
Stroe, A., Shimwell, T., Rumsey, C., et al. 2016, MNRAS, 455, 2402
Stroe, A., van Weeren, R. J., Intema, H. T., et al. 2013, A&A, 555, A110
Stuardi, C., Bonafede, A., Lovisari, L., et al. 2021, MNRAS, 502, 2518
Stuardi, C., Bonafede, A., Rajpurohit, K., et al. 2022, A&A, 666, A8
Stuardi, C., Bonafede, A., Wittor, D., et al. 2019, MNRAS, 489, 3905
Taylor, M. B. 2005, in ASP Conf. Ser. 347, Astronomical Data Analysis Software and Systems XIV, ed. P. Shopbell, M. Britton, & R. Ebert (San Francisco, CA: ASP), 29
Thierbach, M., Klein, U., & Wielebinski, R. 2003, A&A, 397, 53
van Haarlem, M. P., Wise, M. W., Gunst, A. W., et al. 2013, A&A, 556, A2
van Weeren, R. J., Andrade-Santos, F., Dawson, W. A., et al. 2017, NatAs, 1, 0005
van Weeren, R. J., Brüggen, M., Röttgering, H. J. A., et al. 2011a, A&A, 533, A35
van Weeren, R. J., de Gasperin, F., Akamatsu, H., et al. 2019, SSRv, 215, 16
van Weeren, R. J., Hoeft, M., Röttgering, H. J. A., et al. 2011b, A&A, 528, A38
van Weeren, R. J., Röttgering, H. J. A., Brüggen, M., & Hoeft, M. 2010, Sci, 330, 347
van Weeren, R. J., Röttgering, H. J. A., Intema, H. T., et al. 2012, A&A, 546, A124
van Weeren, R. J., Shimwell, T. W., Botteon, A., et al. 2021, A&A, 651, A115
Vazza, F., Brüggen, M., van Weeren, R., et al. 2012, MNRAS, 421, 1868
Wilber, A., Brüggen, M., Bonafede, A., et al. 2018, MNRAS, 473, 3536
Wittor, D., Ettori, S., Vazza, F., et al. 2021, MNRAS, 506, 396
Wittor, D., Hoeft, M., Vazza, F., Brüggen, M., & Domìnguez-Fernández, P. 2019, MNRAS, 490, 3987
Wright, E. L. 2006, PASP, 118, 1711
Xie, C., van Weeren, R. J., Lovisari, L., et al. 2020, A&A, 636, A3
Zhang, X., Simionescu, A., Kaastra, J. S., et al. 2020, A&A, 642, L3